DEUTERON AND ANTIDEUTERON COALESCENCE IN HEAVY-ION COLLISIONS: ENERGY DEPENDENCE OF THE FORMATION GEOMETRY

Apiwit Kittiratpattana

A Thesis Submitted in Partial Fulfillment of the Requirements for the

Degree of Master of Science in Physics

Suranaree University of Technology

Academic Year 2020

ผลของพลังงานต่อรูปทรงเรขาคณิตในการเชื่อมติดเพื่อก่อเกิดดิวเทอรอน
และแอนติดิวเทอรอนในการชนของไอออนหนัก

นายอภิวิชญ์ กิตติรัตน์พัฒนา

วิทยานิพนธ์นี้เป็นส่วนหนึ่งของการศึกษาตามหลักสูตรวิทยาศาสตรปริญญามหาบัณฑิต
สาขาวิชาฟิสิกส์
มหาวิทยาลัยเทคโนโลยีสุรนารี
ปีการศึกษา 2563

DEUTERON AND ANTIDEUTERON COALESCENCE IN

HEAVY-ION COLLISIONS: ENERGY DEPENDENCE

OF THE FORMATION GEOMETRY

Suranaree University of Technology has approved this thesis submitted in partial fulfillment of the requirements for a Master's Degree.

Thesis Examining Committee

_____
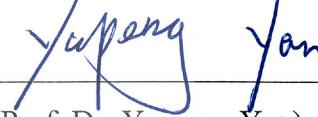
(Prof. Dr. Yupeng Yan)

Chairperson

_____

(Asst. Prof. Dr. Christoph Herold)

Member (Thesis Advisor)

_____

(Asst. Prof. Dr. Ayut Limphirat)

Member (Thesis Co-Advisor)

_____

(Prof. Dr. Marcus Bleicher)

Member

_____
(Assoc. Prof. Flt. Lt. Dr. Kontorn Chamniprasart)

Vice Rector for Academic Affairs

and Internationalization

_____
(Assoc. Prof. Dr. Worawat Meevasana)

Dean of Institute of Science

อภิวิชญ์ กิตติรัตน์พัฒนา : ผลของพลังงานต่อรูปทรงเรขาคณิตในการเชื่อมติดเพื่อก่อเกิด
ดิวเทอรอนและแอนติดิวเทอรอนในการชนของไอออนหนัก (DEUTERON AND
ANTIDEUTERON COALESCENCE IN HEAVY-ION COLLISIONS: ENERGY
DEPENDENCE OF THE FORMATION GEOMETRY) อาจารย์ที่ปรึกษา :
ผู้ช่วยศาสตราจารย์ ดร.คริสทอฟ เฮโรลด์, 72 หน้า.

การชนกันของไอออนหนัก/ดิวเทอรอน/แบบจำลองการเชื่อมติด

เราศึกษาผลของพลังงานต่อการปลดปล่อยดิวเทอรอนและแอนติดิวเทอรอนในช่วง
พลังงานการชนระดับต่ำถึงระดับกลาง หรือในช่วง $\sqrt{s_{NN}} = 7.7 - 200$ จิกะอิเล็กตรอนโวลต์ ซึ่ง
เป็นช่วงที่อัตราการเกิดของแอนตินิวเคลียสถูกยับยั้งอย่างรุนแรงเมื่อเทียบกับอัตราการเกิดของ
นิวเคลียส โดยหลักการของแบบจำลองการเชื่อมติดชี้ให้เห็นว่านิวเคลียสนั้นจะถูกปลดปล่อยทั่วทั้ง
ปริมาตรของลูกไฟ (แหล่งกำเนิด นิวคลีออน) ซึ่งต่างจากกับการปลดปล่อยแอนตินิวเคลียสที่เกิด
บริเวณเปลือกของลูกไฟ เมื่อนำผลการทดลองของตัวแปรการเชื่อมติด B_2 มาเทียบกับแบบจำลอง
และการวิเคราะห์ในวิทยานิพนธ์นี้ เราสามารถถอดรูปทรงเรขาคณิตของแหล่งกำเนิดนิวคลีออน
และแอนตินิวคลีออนได้ วิทยานิพนธ์นี้ยังสนับสนุนหลักการดังกล่าวด้วยผลการวิเคราะห์จาก
แบบจำลอง UrQMD กล่าวคือ สำหรับที่พลังงานการชนต่ำเหล่านิวคลีออนจะเยือกแข็งทั่วทั้ง
ปริมาตรลูกไฟระดับพลังงานต่ำ ในขณะที่เหล่าแอนตินิวคลีออนจะถูกประลัยที่ใจกลางของ
ปริมาตรลูกไฟและเยือกแข็งเฉพาะที่เปลือกของปริมาตร เมื่อพลังงานสูงขึ้นผลกระทบจากการ
ประลัยจะมีความสำคัญน้อยลงเนื่องจากการเพิ่มผลผลิตของเมซอนในปฏิกิริยา ส่งผลให้การเยือก
แข็งของนิวคลีออนและแอนตินิวคลีออนมีลักษณะการแจกแจงที่คล้ายคลึงกันมากขึ้นตามการ
เพิ่มขึ้นของพลังงาน

สาขาวิชาฟิสิกส์

ปีการศึกษา 2563

ลายมือชื่อนักศึกษา _____

ลายมือชื่ออาจารย์ที่ปรึกษา _____

ลายมือชื่ออาจารย์ที่ปรึกษาร่วม _____

APIWIT KITTIRATPATTANA : DEUTERON AND ANTIDEUTERON COALESCENCE IN HEAVY-ION COLLISIONS: ENERGY DEPENDENCE OF THE FORMATION GEOMETRY. THESIS ADVISOR : ASST. PROF. CHRISTOPH HEROLD, Ph.D. 72 PP.

HEAVY-ION COLLISIONS/DEUTERON/COALESCENCE MODEL

We investigate the collision energy dependence of deuteron and antideuteron emission in the RHIC-BES low- to mid-energy range $\sqrt{s_{NN}} = 7.7 - 200$ GeV where the formation rate of antinuclei compared to nuclei is strongly suppressed. In the coalescence picture, this can be understood as bulk emission for nuclei in contrast to surface emission for antinuclei. By comparison with experimental data on the coalescence parameter B_2, we are able to extract the respective source geometries. This interpretation is further supported by results from the UrQMD transport model, and establishes the following picture: At low energies, nucleons freeze out over the total fireball volume, while antinucleons are annihilated inside the nucleon-rich fireball and can only freeze out on its surface. Towards higher energies, this annihilation effect becomes less significant because of the enhanced meson production in the reaction. Thus, the nucleon and antinucleon freeze-out distributions become similar with increasing energy.

School of Physics

Academic Year 2020

Student's Signature _____

Advisor's Signature _____

Co-Advisor's Signature _____

ACKNOWLEDGEMENTS

CONTENTS

CONTENTS (Continued)

LIST OF FIGURES

LIST OF FIGURES (Continued)

LIST OF FIGURES (Continued)

Figure   **Page**

CHAPTER I

INTRODUCTION

Nuclear and Particle physics has been one of the most frontier subjects of science from the discoveries of fundamental particles, i.e., electron, proton, and neutron to the modern physics of quantum mechanics, field theory, the standard model and beyond. Particle scattering experiments help us to probe the structure of an atom or nucleus. This lead to the discovery of strong interaction or strong nuclear force. One of its properties is that it is very much stronger than the Coulomb force at a nucleus scale, i.e., $\leq 2-3$ fm. So protons and neutrons can be attached to form a nucleus without bouncing off from the Coulomb interactions. If we want to look deeper inside of the nucleus (deep scattering), we need a stronger incident beam energy to penetrate the mixed nuclear-coulomb interaction realm to a purely nuclear interaction. Nowadays, physicists all over the world join hands together and develop much better and stronger collision experiments, for example, ee^+-collisions, pA-collisions, and even a few TeV AA-collisions. With high enough energy, the colliding particles/nuclei are torn apart leaving rich fundamental knowledge to be studied and explored.

Relativistic heavy-ion collisions enable us to probe nuclear matter under extreme conditions by colliding energetic heavy nuclei together. The medium created with such extreme conditions, i.e., high temperature (Sarkar et al., 2009), mimics closely the condition at the Big bang, the early state of the universe or neutron star mergers (Rufa et al., 1990). The created medium expands, cools down, and subsequently hadronizes. The quark-soup becomes hadrons (baryon/meson), which could later form light nuclei that flies into a detector to be measured. The production of light (anti)nuclei has been studied by a broad range of scientist from astrophysicists to nuclear-particle physicists in the last years (Hagedorn, 1960; Butler et al., 1961; Nagle

et al., 1996; Schaffner-Bielich et al., 2000; Monreal et al., 1999; L.-W. Chen et al., 2003; Oh et al., 2007; J. Chen et al., 2018). The abundance of light (anti)nuclei could give us many insightful information about our universe and especially the heavy-ion collisions experiment. It could give us an answer to why our universe contains much less antimatter than normal matter since the Big bang nucleosynthesis (Malaney et al., 1993). In heavy-ion collisions, nucleosynthesis happens at the later stage of the collisions. The formation of light nuclei also enables us to extract properties of the Quark-Gluon Plasma (QGP) (DeGrand, 1984), the probability and formation mechanism for exotic nuclei or hypernuclei (Rufa et al., 1990; Zhu et al., 2015), and the equation of state for cosmological objects. In this thesis, we will focus on the study of deuteron formation which is the simplest nucleon-nucleon composite particle and could serve as a basis for any future study on light nuclei, e.g. tritium and helium. The light nuclei and deuteron subject will be discussed in chapter II.

To understand and predict the formation rate of light nuclei, one can directly calculate from quantum chromodynamics (QCD). QCD explains the dynamics of the color charge between individual quarks at a microscopic level. Unfortunately, it is almost impossible to solve this enormous many-body interacting system produced in each collision. One can still go through microscopic calculations by focusing on the quantum mechanics such as sudden approximation, perturbation theory (Jennings et al., 1982) and transport model (Bleicher, Hillmann, et al., 2020; Sun and Ko, 2020). However, we want to focus on a statistical macroscopic picture. The two most popular statistical models are the thermal model (Gosset et al., 1977; A. Z. Mekjian, 1978; Kapusta, 1980) which treats each particle species as a unique degree of freedom in the fermion/boson gas, and the coalescence model, i.e., formation from localized (anti)nucleons in phase-space coordinates (Mrówczyński, 2017; Steinheimer et al., 2012; Aichelin et al., 1987; Sato et al., 1981). Both are based on the same statistical approach. Their mechanisms are fundamentally different in the interpretations which

will be reviewed in detail in chapter III.

The simple coalescence model has been successful for decades but failed to predict the antideuteron production in Si-Au collisions at AGS in 1992 (Aoki et al., 1992). This reflects the difference in the formation of both particles. After many arguments, it has been shown that the main problem is that the deuteron and antideuteron formation rates are sensitive to the source shape (Sato et al., 1981; Leupold et al., 1994). Thus the simple coalescence, which is mainly based on the phase-space formation, fails. Then in 1993, the author of (Mrówczyński, 1993) applied the spatial geometry into the coalescence model. The main assumption is that the antinucleons are emitted only from the outer shell of the source due to a high probability of nucleon-antinucleon annihilation in the central baryon-rich region. On the other hand, nucleons are emitted from the whole volume. The model assumes a spherical symmetry and was validated by experimental data from Si+Au collisions at $E_{lab} = 14.6$ GeV.

After years of experiments, we have gained more statistics for the deuteron and antideuteron formation rates at different energies. In this work, we improve Mrówczyński's coalescence model with his minor calculation and further the idea to extract the spatial geometries of nucleon and antideuteron source at beam energies from $\sqrt{s_{NN}} = 7.7 - 200$ GeV. Since the deuteron and antideuteron formation are sensitive to space-time geometries, it would be helpful to know how the sources grow as a function of energy, such that we could explain why and how the (anti)deuteron, or ultimately (anti)light nuclei, are produced. In chapter IV and V, we present our approaches how to extract the source geometries analytically and numerically. Firstly, we apply Mrówczyński's coalescence model directly to the calculation. In this aspect, any suppression in the nucleon source is neglect. Then in a second method, we put constraint to the root-mean-squared radius of the nucleon source via the number of charged particles. With this second approach, both nucleon and antinucleon sources will have non-zero suppression at the central core.

Recently, deuteron production from the coalescence model has been studied within the Ultra-relativistic Quantum Molecular Dynamics model (UrQMD) (Bass et al., 1998). The UrQMD transport model is a microscopic transport model based on binary scattering of hadrons, resonance excitations, resonance decays, and string dynamics as well as strangeness exchange reactions. The deuteron rapidity and transverse momentum distributions as well as the d/p and $\bar{d}/\bar{p}$ ratios are in agreement with experimental data (Sombun et al., 2019). The model presented in this thesis, Mrówczyński's coalescence model, assumes instantaneous emissions. Thus it could overestimate the yields. In chapter VI, we show how we apply the UrQMD to simulate the collisions at different energies and obtain freeze-out coordinates of nucleons and antinucleons.

Finally, we will conclude the thesis in chapter VII. The results as well as the suggestions for possible future work and interesting questions and ideas will be discussed here.

CHAPTER II

REVIEWS ON LIGHT (ANTI)NUCLEI

The exploration of cluster formation in nuclear reactions started more than 50 years ago (Hagedorn, 1960; Butler et al., 1961) and has been continued since then (Nagle et al., 1996; Schaffner-Bielich et al., 2000; Monreal et al., 1999; L.-W. Chen et al., 2003; Oh et al., 2007; Zhu et al., 2015; J. Chen et al., 2018). The physics of light (anti)nuclei has already a long history covering a broad scientific range from astrophysics, e.g., Big Bang nucleosynthesis (Malaney et al., 1993), hypermatter in neutron stars (Rufa et al., 1990) or signals of dark matter annihilation (Wiringa et al., 2014; Korsmeier et al., 2018) to nuclear-particle physics (Braun-Munzinger and Dönigus, 2019) and even physics beyond the standard model (Beyer, 1993; Aid et al., 1995). In this chapter, we will start by giving a review of the standard model for particle physics.

2.1 The Standard Model

The most elementary particles known today are not only at the level of atoms or protons and neutrons. The standard model of elementary particle physics describes the fundamental building blocks of matter along with the interaction forces that govern them. The currently known elementary particles are classified into two groups; leptons and quarks. Another group representing the exchange particles for the force carriers, are the bosons. These are shown in Figure 2.1.

Both quarks and leptons are fermions that obey Fermi-Dirac statistics. Fermions have half-integer spin. On the other hand, bosons have integer spin and obey Bose-Einstein statistic. Gauge bosons have a spin of 1. Photons carry elec-
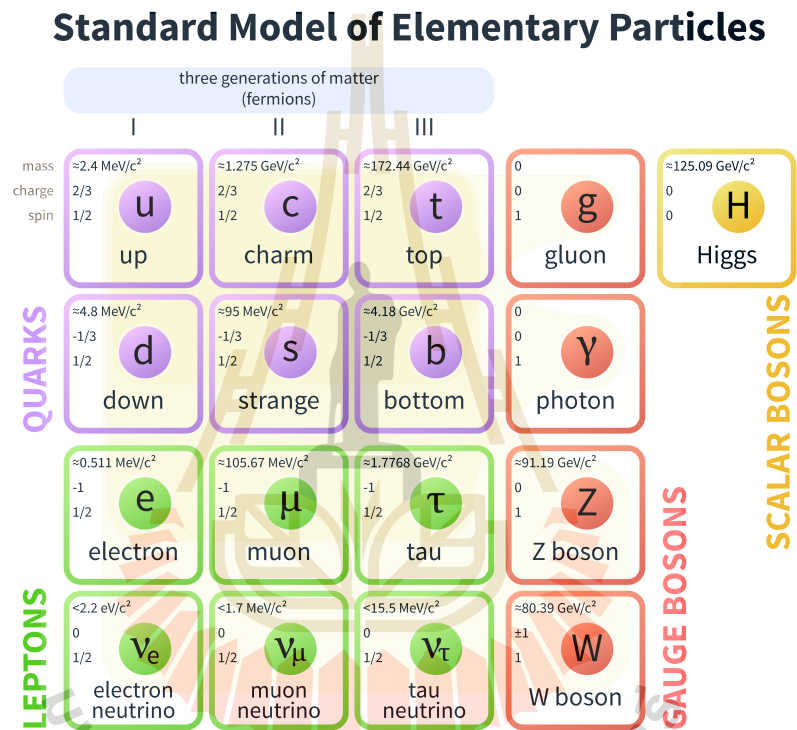
Figure 2.1 The Standard Model of elementary matter particles, with the three generations of matter(quarks and leptons), gauge bosons(force carriers) in the fourth column, and the Higgs boson in the fifth (Fehling, 2008).

tromagnetic interaction. W and Z bosons, carry the weak interaction, gluons, carry the strong interaction. There are six flavours of quarks; up (u), down (d), charm (c), strange (s), top (t), bottom (b). Quarks have various intrinsic properties, including electric charge, mass, spin. Up and down quarks have the lowest masses of all quarks. The heavier quarks are unstable. They rapidly change into up and down quarks through a process of particle decay. Up and down quarks are stable and the most common in the universe, whereas strange, charm, bottom, and top quarks can only be produced in high energy collisions (such as those involving cosmic rays and in particle accelerators). Furthermore, quarks are the only elementary particles in the Standard Model of particle physics to experience all four fundamental interactions (electromagnetism, gravitation, strong interaction, and weak interaction). The interaction between quarks and gluons is described by the dynamics of color charge, which is called "Quantum Chromodynamics" (Fritzsch et al., 1972).

Nowadays, the theoretical tools for nuclear and particle physicists are abundant and successful. However, it is still difficult to describe and predict such enormous many-body dynamics problem of nuclear reactions in heavy-ion collisions based on these theories.

Protons and neutrons are known as nucleons depicted by their role in the nuclei. The isotope mass number of an atom is defined by how many nucleons they are carrying. A proton is composed of two up quarks and one down quark, while the neutron has one up quark and two down quarks. The summed up spin of quarks in either type of nucleon is 1/2 and thus nucleons are fermions. The masses of the proton and neutron are very similar: The proton is carrying a rest-mass of 938.27 MeV, while the neutron is carrying 939.57 MeV.

Light (anti)nuclei are the most simple nucleon-nucleon compound particles e.g. deuteron (d), triton (t), helium-3 (He^3), helium (α), and etc. Deuteron, d, is known as heavy hydrogen H^2 nucleus which contains one proton and one neutron. Its binding

energy is around 2.2 MeV. Most natural deuterons, either on Earth, planets, or comet, are produced from the Big Bang 13.7 billion years ago. Triton is the nucleus of a rare hydrogen isotope, tritium H^3, consists of one proton and two neutrons. helium-3 or He^3 contains two protons and one neutron which is a stable isotope of helium. Helium nuclues or $\alpha-$particle has two protons and two neutrons. All of these light nuclei can decay and produce one after another in a chain reaction. Hence, one could see the importance of these light nuclei to the evolution of nuclear reactions, more review (J. Chen et al., 2018; Oliinychenko, 2021).

2.2 Evolution of Universe

In this section, we will introduce the importance of the formation of light nuclei especially deuterons. From two different points of view. Firstly we will start with the cosmological point of view, how these light nuclei play an important role in the evolution of the universe and inside of the astronomical objects such as stars followed by the experimental point of view which nuclear and particle physicists are actively interested in.

The Big Bang model of the early universe is currently the most reliable model for explaining the evolution of our universe from the initial singularity. It has undergone many different phases and epochs. In the early universe, the temperature and the density were extremely high leading to extremely fast and violent transitions. Fortunately, these processes could be studied epoch by epoch thanks to general relativity, the standard model of particle physics, and the thermodynamics description to understand and track back how each phase progressed.

The interesting thing is that the atomic nuclei that formed in the early universe come from the primordial gas hydrogen and helium. Then, these most simple light nuclei fuel nuclear fusion inside the star producing other nuclei, e.g., helium-3, lithium. Since the deuterium source was only at the Big Bang nucleosynthesis, the formation

of deuteron could be used as an important footprint from the Big Bang. This is also true for the formation of light nuclei at the later stage of the collision.

2.2.1 Big Bang Nucleosynthesis

The theory of light element formation in Big Bang nucleosynthesis started in 1940 in the $\alpha\beta\gamma$ paper (Alpher et al., 1948). At the Big Bang nucleosynthesis, the temperature is cold enough for protons and neutrons to form into nuclei. Deuterons consist of one proton and one neutron. Then these deuterons fuse with more protons or neutrons becoming triton or helium-3 and so on through nuclear chain reaction resulting in different light nuclei abundance. Figure 2.2 shows the mass fraction of light nuclei and isotopes to the total mass of the universe vs time and temperature during the Big Bang nucleosynthesis. After the lepton epoch, the leftover protons and neutrons interact with leptons and positrons generating neutrinos through weak interactions. However, the temperature, as well as the number of photons, are still too high to produce any stable nuclei. Neutrons change into protons via $\beta-$decays. Here, the neutron:proton ratio becomes around $1:7$ from $1:6$.

$$p + e^- \rightarrow n + \nu$$
$$n + e^+ \rightarrow p + \bar{\nu}$$
$$n \rightarrow p + e^- + \bar{\nu}$$
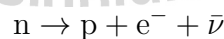
At few 100 seconds pass, the temperature is low enough for deuteron formation to occur. The preserved neutrons were captured by protons in deuteron formation and ignited the nucleosynthesis with nuclear chain reaction resulted in the strong
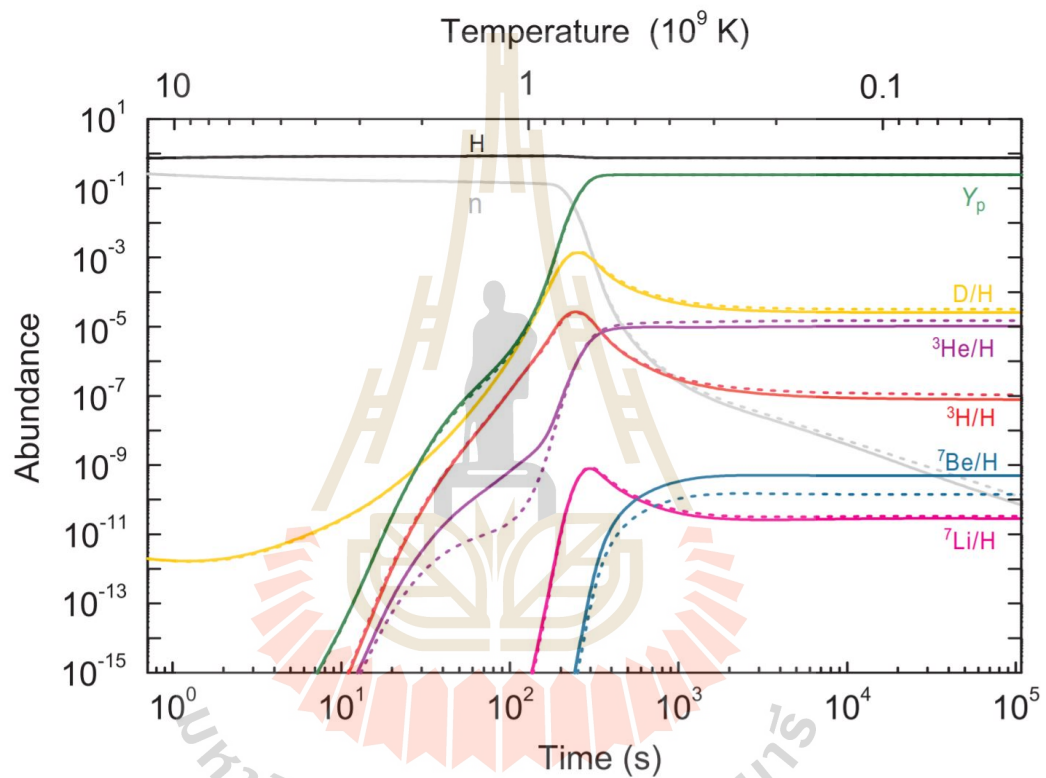
Figure 2.2 The abundance of light elements in the early universe as a function of time and temperature. The lower/upper limit are presented by the dotted lines and the Maxwell-Boltzmann predictions are shown with solid lines (Hou et al., 2017).

increasing of all isotopes.

$$p + n \rightarrow d + \gamma$$

$$d + n \rightarrow H^3 + \gamma$$

$$H^3 + p \rightarrow He^4 + \gamma$$

$$d + p \rightarrow He^3 + \gamma$$

$$He^3 + n \rightarrow He^4 + \gamma$$
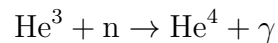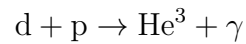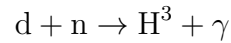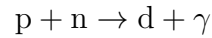
After that the temperature fell to around 0.1 MeV, those above reactions eventually died down toward helium production after the so-called deuteron bottleneck where the deuteron abundance was at the peak. Because helium is more bounded than deuteron with an energy of around 28 MeV, the nuclear reaction could not occur further. Furthermore, the lower density of the universe also prevents the formation of deuteron as the Coulomb repulsion between protons dominates the strong force. Thus we can think of helium as ashes from the combustion and deuteron as fuel.

$$d + d \rightarrow He^3 + n$$

$$d + d \rightarrow H^3 + p$$

$$H^3 + d \rightarrow He^4 + n$$

$$H^3 + d \rightarrow He^4 + p$$
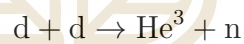
At the end of nucleosynthesis, the net product could be understood such that, most of survived neutrons end up as deuterons. Then most of these deuterons fuse with nucleons and/or He^3 becoming He^4. The mass fraction ratio helium:proton is around 1:4 or 25%.

$$n \rightarrow d \rightarrow He^4$$
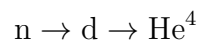
Since there is no other natural process to produce deuterons, this makes the number of deuterons an important parameter to the limit of other baryonic masses

of our universe. Although one can argue that the deuteron is producible in stellar nucleosynthesis, the main differences between Big Bang nucleosynthesis and stellar nucleosynthesis are that the latter has no free neutron in the process. Nuclear fusion happens much slower in this case as it needs higher energy to overcome the coulomb repulsion. Furthermore, space and time conditions also very different. In the Big Bang nucleosynthesis, the density, as well as the time scale, are much more extreme. Stellar nuclear fusion happens in a very long time i.e. millions of years. And in this condition, deuterons cannot survive and could only fuel the fusion process. One can say deuteron formation depends on the initial conditions than helium, especially in space and time aspects. Hence this marks the uniqueness of deuteron to the Big Bang nucleosynthesis or similarly to heavy-ion collisions.

2.3 Heavy-ion Collisions

In the last 20 years, heavy-ion collisions have been a unique way to study the hadronic matter in the laboratory. The nuclear matter or QCD phase diagram remains unknown, although many experimental and theoretical studies have been undertaken in the last decades. After the initial experiences accelerating heavy nuclei onto fixed targets at the AGS (BNL, USA) and the SPS (CERN, Switzerland), the Relativistic Heavy Ion Collider (RHIC) at BNL was the first ever built heavy-ion collider. RHIC delivered its first collisions in 2000 creating excitement for the heavy-ion community. In 2010, the Large Hadron Collider (LHC) at CERN delivered lead-lead collisions at unprecedented center-of-mass energies, 14 times larger than that at RHIC. These experiments have already given us many intriguing results (Martinez, 2013). Needless to say that the heavy-ion programs at RHIC and LHC promise more fascinating and exciting results in the next decade.

When two high-energy heavy ions collide, the collision creates a very hot and dense medium, a fireball of a fluid-like medium. Then this hot fireball expands and
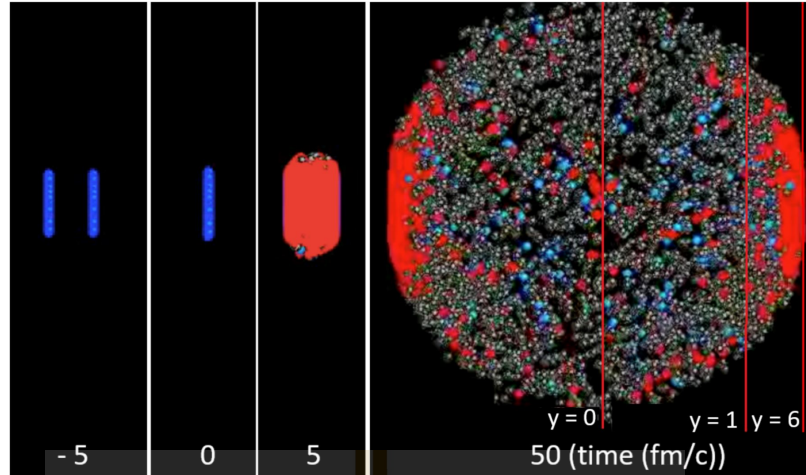
Figure 2.3 (a). Two heavy-ion flattened into a pancake shape since they are traveling near the speed of light. (b). At zero time, both nuclei collide each other. (c). Protons and neutrons dissolve for a brief instant, liberating their constituents (quarks and gluons) to form a Quark gluon plasma (very hot and dense fireball) (d). The quark-gluon plasma subsequently decays into thousands of particles. Each of these particles provides information as a footprint to what occurred inside the collision zone (Busza et al., 2018).

cools down undergoing a phase transition from quark-gluon plasma to hadron gas, see figure 2.3. This evolution will be shown in the space-time picture in the next section.

As soon as the system is in local thermal equilibrium, its evolution can be described by relativistic hydrodynamics (Monnai, 2014), where instead of single particles, energy and baryon densities are propagated according to the corresponding conservation laws. The hydrodynamic stage is especially interesting as it comprises not only the evolution of the QGP but also the subsequent phase transition to the hadrons. At some time τ_f, the hadrons will cease to interact and stream freely into the detector where they are measured. This is called the freeze-out. More precisely, one distinguishes between two types of freeze-out: first comes the chemical freeze-out, after which no inelastic collisions occur anymore, resulting in the fixed chemical composition of the system. Then, at the moment when elastic collisions cease as well,
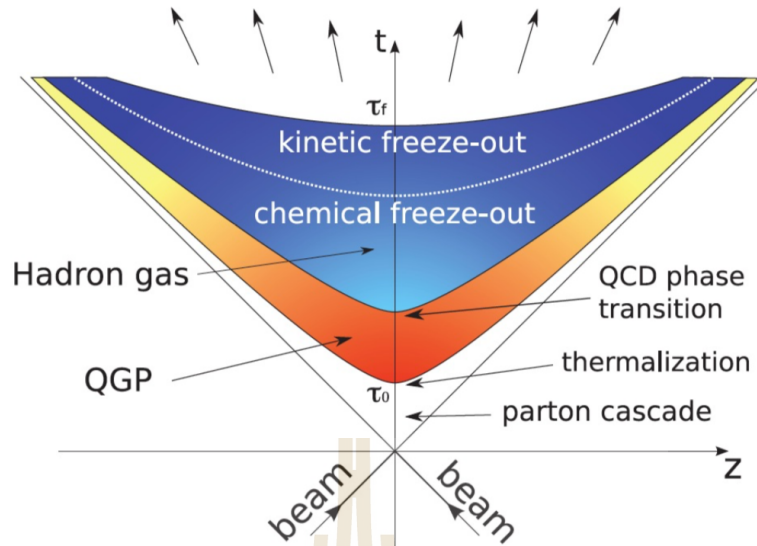
Figure 2.4 The space-time evolution of a heavy-ion collision according to the Bjorken model. (Shi et al., 2009; Bjorken, 1983).

one speaks of a thermal or kinetic freeze-out. From the definition, it is clear that the chemical freeze-out will happen before the kinetic freeze-out.

2.3.1 Potential Signal of Critical Point

Another reason to study light nuclei production is the search for the critical point of strongly interacting matter. Quarks possess an intrinsic property called color charge. There are three types of color charge, red (r), green (g), blue(b). Each of them is complemented by an anticolor — antired($\bar{r}$), antigreen($\bar{g}$), antiblue($\bar{b}$). Every quark carries a color, while every antiquark carries an anticolor. The interaction of attraction and repulsion between color charges is called strong interaction, which is mediated by force-carrier particles known as gluons. The theory that describes strong interactions is called quantum chromodynamics (QCD).

The very first idea of a QCD phase diagram was purposed by N. Cabibbo and G. Parisi (Cabibbo et al., 1975) and after years of studying a diagram has become more developed as shown in figure 2.5. One phase is called a hadronic phase or
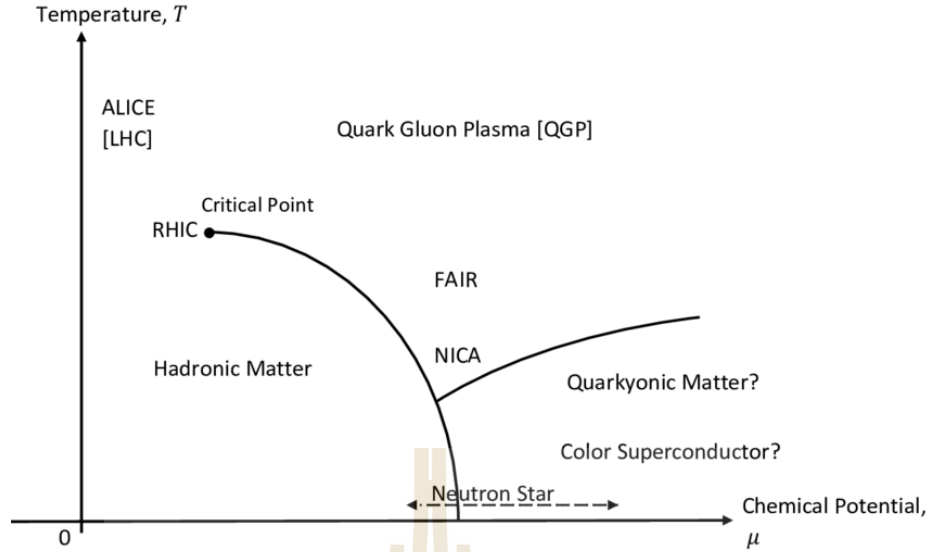
Figure 2.5 The sketch of QCD phase diagram as a function of temperature T (MeV) and baryon chemical potential μB (McInnes, 2016).

color confinement which the domain of low density μ and temperature T. Due to a phenomenon known as color confinement, quarks are never directly observed or found in isolation but confined in colorless hadrons. Hadrons are particles including mesons and baryons. Mesons are composed of quark-antiquark, e.g., π(pion). Baryons are composed of three quarks, e.g., proton and neutron. Another phase is called quark-gluon plasma (QGP) characterized at sufficiently high temperatures, quarks and gluons interact weakly, and the system will behave as an ideal ultra-relativistic gas or fluid (Herold et al., 2019) as known as QGP. The line separating between these two phases at low $\sqrt{s_{NN}}$ and/or high μ is the first-order phase transition which could be reached by energy ranges at GSI-FAIR, NICA. At the end of this line, we have a predicted critical end point that has been studied theoretically and experimentally in recent years. After the critical end point at low μ, we have a smooth cross over which also applies to the evolution of the early universe. Currently, only LHC and RHIC at CERN can reach these extreme conditions with heavy-ion collisions. For higher μ, there are also possible novel phases of Color Superconductor and Quarkyonic Matter at $T \to 0$ MeV (McLerran et al., 2007).

The evidence for the existence of the QGP phase has been studied intensely and the results are very positive. However, the boundary between these two phases is still unclear. Whether or not, is there a critical end point of the first-order phase transition?

It has been argued that the enhanced long-wavelength fluctuations near the CEP lead to singularities in all thermodynamic observables (Stephanov et al., 1998). The resulting event-by-event fluctuations of conserved quantities in relativistic heavy-ion collisions have thus been extensively studied both theoretically and experimentally. For example, the energy dependence of the fourth-order fluctuation ($\kappa\sigma^2$) of net-proton distribution measured in the BES program by the STAR Collaboration found a large deviation from unity in Au+Au collisions at $\sqrt{s_{NN}} = 7.7$ GeV (N. Xu, 2018). In the case that such density fluctuations can survive final state interactions during the hadronic evolution of heavy-ion collisions, strong fluctuations in the nucleon density and thus significant inhomogeneities in the spatial distribution of nucleons are expected at kinetic freeze-out. Therefore, the nucleon density fluctuations at kinetic freeze-out in relativistic heavy-ion collisions may provide a unique probe to the critical endpoint in the QCD phase diagram, where, spatial fluctuations of the nucleon density are enhanced. Although spatial fluctuations are not measurable directly (Sun, L.-W. Chen, et al., 2018).

CHAPTER III

STATISTICAL APPROACHES FOR LIGHT (ANTI)NUCLEI FORMATION

In this section, we will introduce recent models for light (anti)nuclei production mechanism. The models/mechanisms can be divided into two groups: models taking the wave function and quantum effect into consideration and models based on statistics. The example of the first category is, for instance, the sudden approximation model. This model can be applied if one assumes that the cooling down process of the transition occurs rapidly. That is when the high density and excitation energy stage change to the low-density stage. The proton-neutron pairs start to develop correlation and form into deuterons. The transition probabilities of the initial stage and final state should be approximately the same. With this fact, one can calculate the probabilities from the overlap of both wave functions. The involved volume also is one of the interesting parameters to be studied. For the second category, the most successful statistical models of light (anti)nuclei productions are the thermal model and the coalescence model, which will be focused on and reviewed below, in subsections 3.1 and 3.2. We will follow the explanation presented by Joseph I. Kapusta (Kapusta, 1980).

3.1 Thermal model

When dealing with the physics of many-body problems, the thermal model is the first tool to be thinking of. Thermodynamics models have successfully gained their standing in the relativistic heavy-ion collisions domain. We have been extensively using these models to study the macroscopic properties of strongly interacting

matter in the board range energies, especially in extreme conditions. The Quantum Chromodynamics (QCD) predicts the possible nuclear matter phase transition, i.e., hadron gas to Quark-Gluon-Plasma (QGP). The statistical thermal model is applicable when the system or the collisions has reached equilibrium and chemical freeze-out. We can characterize this system by temperature and chemical potential. In this section, we will introduce the setup of the model for light (anti)nuclei production and discuss some drawbacks.
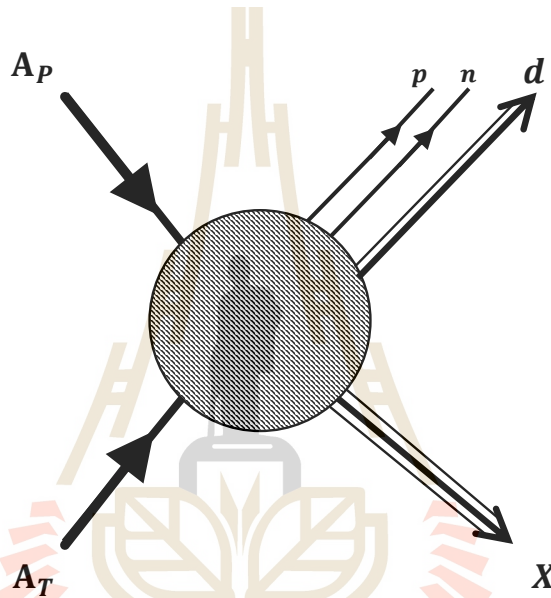
Figure 3.1 The schematic for a particle production from the fireball created by a projectile nucleus A_P and a target nucleus A_T. In thermal model, the particles, p and n, are emitted directly from the fireball including the composited particle and the rest of the momentum X, e.g., (anti)deuteron d.

The basic idea ofthe thermal model is to treat various species of particles as a non-interacting gas system. The schematic for the thermal model is shown in figure 3.1.

In side the fireball, all kinds of particles (nucleons, pions, etc.) can be produced and composite particles (d, t, He etc.) can be formed. The nucleons and deuterons are treated as free particles inside a box of volume V characterized by temperature

T and chemical potential μ_i. Then the distribution of particle i can be described as,

$$\frac{d^3 n_i}{d\mathbf{p}_i^3} = \frac{(2S_i + 1)}{(2\pi)^3} V \left[\exp\left(\frac{(\mathbf{p}_i^2 + m_i^2)^{1/2} - \mu_i}{T} \right) \pm 1 \right]^{-1}, \qquad (3.1)$$

where S_i is the spin multiplicity of the particle and $\pm$ depends on the particle species; fermion or boson. With the ansatz and our observation, the deuteron production is proportional to the square of nucleons density,

$$\frac{d^3 n_d}{d\mathbf{P}} = \frac{3}{4} \frac{(2\pi)^3}{V} \frac{d^3 n_p}{d\mathbf{p}_1^3} \frac{d^3 n_n}{d\mathbf{p}_2^3}, \qquad (3.2)$$

with deuteron momentum $\mathbf{P} = \mathbf{p}_1 + \mathbf{p}_2$ assuming proton and nucleon to share the same momenta $\mathbf{p}_1 = \mathbf{p}_2 = \mathbf{p}$. The weighing factor of $3/4$ is to average the spin multiplicity per nucleon-nucleon bound state. Written in Lorentz invariant density form, gives

$$\left(\gamma \frac{d^3 n_d}{d\mathbf{P}} \right) = 8 \frac{3}{4} \frac{(2\pi)^3}{V} \frac{1}{\gamma} \left(\gamma \frac{d^3 n_p}{d\mathbf{p}} \right)^2. \qquad (3.3)$$

These deuteron distributions seem to be alright as they are in the momentum space. This thermal description can provide a good estimate for the light nuclei and hadron production. See figure 3.2. This may see as the overestimated of antineutron or otherwise for the deuteron. On the other hand, the number of (anti)proton and charged pions matches quite well. Almost all composited particles can be fitted nicely with a thermal model from SPS to RHIC energy without any need to introduce more parameters (Braun-Munzinger, Magestro, et al., 2001; Braun-Munzinger, Redlich, et al., 2004).

Ultimately, one could raise a question on this thermal prescription. How could the deuterons exist inside the fireball? The binding energy of deuteron, a weakly bound particle, is much lower than temperature of the medium created by ultra-relativistic heavy-ion collisions. Nevertheless, since the thermal model does not de-
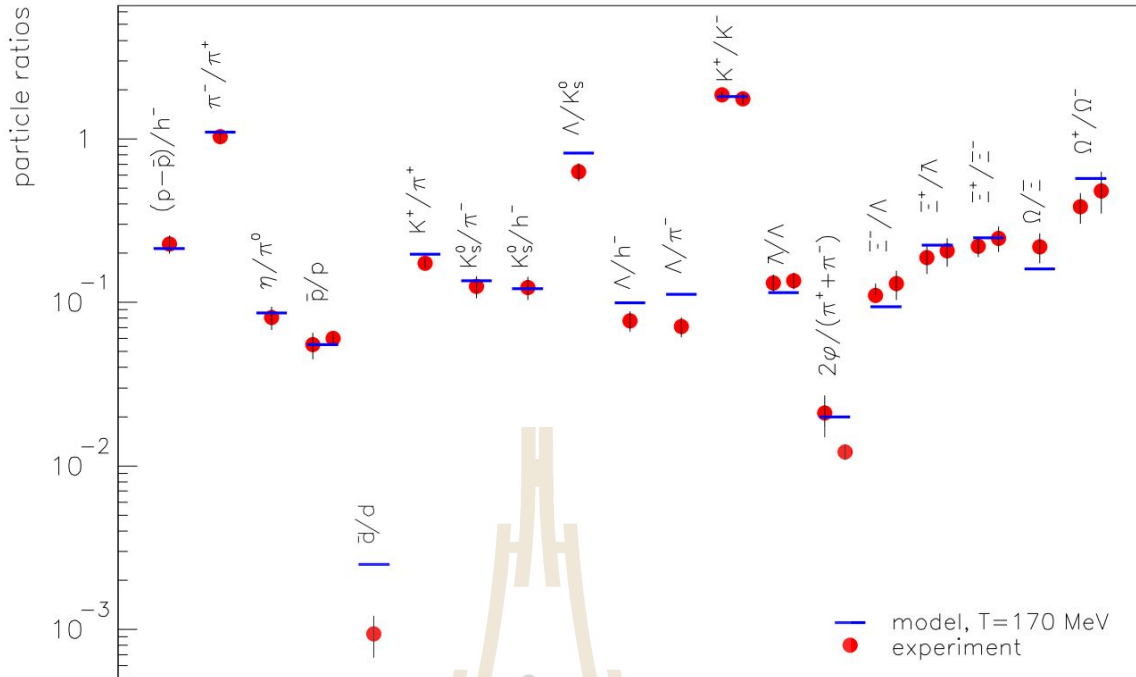
Figure 3.2 The comparison between thermal model predictions and the experimental particle ratios for Pb–Pb collisions at 158 GeV/nucleon (Adler et al., 2001; Specht, 2002; Z.-b. Xu et al., 2001; Soff, 2002; Back et al., 2001; Bearden et al., 2001).

scribe any microscopic dynamics and purely statistics, the results on the macroscopic picture are in agreement with the experiments. In contrast to the thermal model, the coalescence model assumes the mechanism on how the light nuclei are formed which has a different view on where the light (anti)nuclei are produced, i.e., outside of the fireball.

3.2   Coalescence Model

The coalescence model describes the formation of baryonic clusters in the late stage of a collision — first all resonances decay into nucleons, then nucleons coalesce into nuclei at the freeze-out stage. They are many kinds of coalescence models; nucleon power's law, Wigner's function, etc. The model says a pair of final-state (anti)nucleons that are carrying similar momenta can coalesce to form a deuteron or
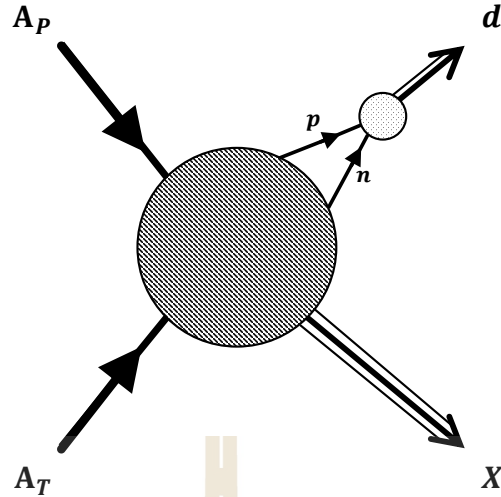
Figure 3.3 The schematic for a deuteron production in the relativistic heavy-ion collision. A_P and A_T represents the projectile and target nucleus. p and n are a proton and a neutron, while d is a deuteron. X is the rest of the momentum of the system.

an antideuteron with total momentum $\mathbf{P}$ as shown in figure 3.3. Different formulations for the coalescence rate are possible. In this section, we will present the idea and discuss the problems of the simple coalescence model which motivates the need for an alternative consideration to the model.

3.2.1 Simple coalescence

The coalescence model for relativistic nuclear collisions was developed from the physical insight provided by proton-nucleus collisions by Butler and Pearson. Then, Schwarzschild and Zupancic pointed out that, independent of the detailed production mechanism, the deuteron density $d^3 n_d/d\mathbf{p}$ should be proportional to the square of the proton density $[d^3 n_p/d\mathbf{p}]^2$. The coefficient may be momentum-dependent and could be made dependent on details of the mechanism.

The derivation of the coalescence model for deuterons goes as follows. Let $d^3 n_p/d\mathbf{p}$ be the invariant momentum-space density for nucleons before coalescence

into deuterons. We assume that protons and neutrons have equal densities but the formulas can be generalized to include the non-equal cases. Consider a sphere in momentum space centered at p_0 and with a radius $\mathbf{p}$ The probability for finding one primary nucleon in this sphere is

$$P = \frac{1}{M}\frac{4\pi}{3}p_0{}^3\gamma\frac{d^3n_p}{d\mathbf{p}} \ , \tag{3.4}$$

where M is the mean nucleon multiplicity. The purely statistical probability for finding two nucleons in the case where $M >> 1$ and $MP >> 1$ of this sphere is

$$P_M(2) = \binom{M}{2}P^2(1-P)^{M-2}. \tag{3.5}$$

$$\frac{4\pi}{3}p_0^3\gamma\frac{d^3n_d}{d\mathbf{P}} = \frac{M^2}{2}\left(\frac{1}{M}\frac{4\pi}{3}p_0^3\gamma\frac{d^3n_p}{d\mathbf{p}}\right)^2 \ , \tag{3.6}$$

$$\gamma\frac{d^3n_d}{d\mathbf{P}} = \frac{1}{2}\frac{4\pi}{3}p_0^3\left(\gamma\frac{d^3n_p}{d\mathbf{p}}\right)^2 . \tag{3.7}$$

If we consider the spin and isospin multiplicity, one could get,

$$\gamma\frac{d^3n_d}{d\mathbf{P}} = 8\frac{3}{4}\frac{4\pi}{3}p_0^3\left(\gamma\frac{d^3n_p}{d\mathbf{p}}\right)^2 \ , \tag{3.8}$$

again where deuteron momentum $\mathbf{P} = \mathbf{p}_1 + \mathbf{p}_2$ and proton and neutron share the same momenta $\mathbf{p}_1 = \mathbf{p}_2 = \mathbf{p}$. Mathematically this model says that whenever a proton and a neutron are within a momentum p_0 of each other and in the correct spin state then they will coalesce. Note that this equation contains only the invariant density, the equation itself is not a Lorentz invariant. Usually, the coalescence model, in general, is written in the form of invariant cross-section,

$$E\left(\frac{d^3\sigma_A}{d\mathbf{P}}\right) = B_A\left(\frac{E}{A}\frac{d^3\sigma_p}{d\mathbf{p}}\right)^A \ , \tag{3.9}$$

assuming the equality of cross-section of the nucleons. A is the number of nucleons for any light nucleus. E is the energy of the light nucleus where the nucleons's are

assumed to energy E/A. B_A is a well-known coalescence parameter which is used in most of the experiments related to the coalescence model. Still, B_2, of deuteron for example, also contains the proportionality to the unknown p_0. However, the interpretation of radius p_0 in phase space is still questionable. Because this parameter could not be explained with any dependencies on the collision initial conditions, e.g., the target/projectile size, beam energy, impact parameter, and etc.

Comparing this the eq. (3.8) with the thermal model eq. (3.3), we get the relation for p_0,

$$\frac{4}{3}\pi p_0^3 = \frac{1}{\gamma}\frac{(2\pi)^3}{V} \tag{3.10}$$

Even with this relation, p_0 seems to be inversely proportional to the thermal volume V and the Lorentz factor γ. This could lead to the misconception since one needs to know where the center of mass frame is and/or are there more than one emitting system.

Also, because of its simplicity, the model fails to describe the production of antideuterons at Si+Au in the AGS experiment E802 (Aoki et al., 1992). Figure 3.4 shows the invariant cross-section of the negatively charged particles and antinuclei produced in the collisions. The cross-section ratio of antideuteron to antiproton squared, the antideuteron formation rate is $5-10$ times smaller than the deuteron formation rate. Since the simple coalescence rules the production mechanism mainly by the momentum radius p_0 in phase space, then the formation of deuterons and antideuterons should be roughly the same.

From the density matrix formalism (Sato et al., 1981) or a thermal framework (A. Mekjian, 1977), the formation rate should depend on the size and shape of the emission-source region. Furthermore, it has been argued that the formation rates of antideuterons (Mrówczyński, 1990; Dover et al., 1991; Leupold et al., 1994) reflect the
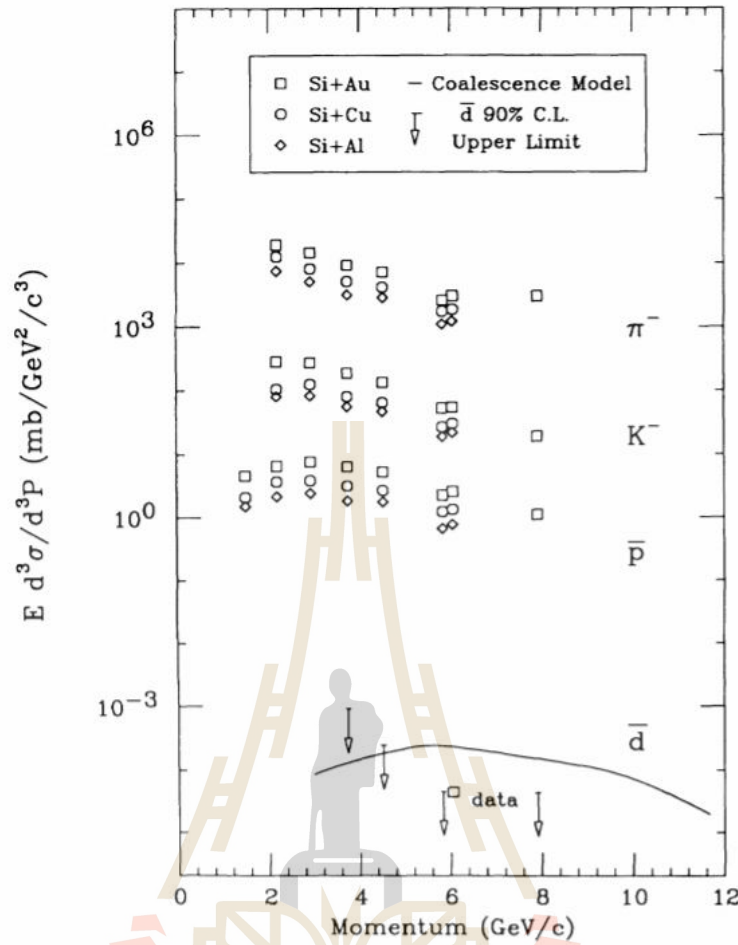
Figure 3.4 The particle invariant cross section spectra for $\pi^-, K^-, \bar{p}$ and $\bar{d}$ from Al, Cu, and Au targets. The solid-line represents the $\bar{d}$'s predicted by coalescence model. The $\bar{d}$'s 90%-C.L. upper limits in the invariant cross section is dictated by the instruments. The measured $\bar{d}$ data point is shown at 6.1 GeV (Aoki et al., 1992).

space-time characteristics of particle sources in nuclear collisions, i.e., the difference in the source geometry. Then S. Mrówcyńzski purposed the space-time formation rate consideration and applied it to the coalescence model. Which will be presented in the following section.

3.2.2 Mrówczyński coalescence model

The model aims to address the failure of the simple coalescence model presented by Si-Au Collisions at AGS. In this alternative model, the shape of the

(anti)nucleons source has been reconsidered and the immeasurable parameter p_0 was eliminated. The (anti)deuteron distributions and (anti)nucleon distributions are now depending on an adjustable space-time parameter which can be related to the collision system initial conditions. In this section, we will follow the explanation and the prescription from his original paper (Mrówczyński, 1993).

The main assumption is that the antinucleons produced near the center of the interaction region of the collision have a very high probability to experience secondary interactions and annihilate in the baryonic environment. While antinucleons produced on the outer surface, can survive and fly out of the fireball for coalescence, nucleons are emitted from the whole source or fireball volume. From the above picture, the different shapes of antinucleon and nucleon sources can help us explain the difference between the formation rates. The cross-section of (anti)deuteron formation can be written as,

$$\frac{d\sigma_d}{d^3\mathbf{P}} = \mathcal{A}' \frac{d\tilde{\sigma}_{np}}{d^3\mathbf{p}_1 d^3\mathbf{p}_2} \ , \tag{3.11}$$

where $\mathcal{A}'$ is the formation rate in lab frame and $\frac{d\tilde{\sigma}_{np}}{d^3\mathbf{p}_1 d^3\mathbf{p}_2}$ is the n-p production cross section with $\mathbf{p}_1 = \mathbf{p}_2 = \mathbf{P}/2$. By neglecting the particle correlations at the final state of collisions, it can be factorized as

$$\frac{d\tilde{\sigma}_{np}}{d^3\mathbf{p}_1 d^3\mathbf{p}_2} \propto \frac{d\sigma^n}{d^3\mathbf{p}_1} \frac{d\sigma^p}{d^3\mathbf{p}_2} \ , \tag{3.12}$$

with σ^{inel} being the total inelastic cross-section.

In the particle source rest frame, the deuteron formation rate $\mathcal{A}' = \gamma\mathcal{A}$ with γ being the Lorentz factor of the deuteron motion. The formation rate is

$$\mathcal{A} = \frac{3}{4}(2\pi)^3 \int d^3r_1 d^3r_2 \mathcal{D}(\mathbf{r}_1)\mathcal{D}(\mathbf{r}_2)|\psi_d(\mathbf{r}_1, \mathbf{r}_2)|^2, \tag{3.13}$$

where the source function $\mathcal{D}(\mathbf{r})$ describes the probability of finding a nucleon at a given point $\mathbf{r}$ at kinetic freeze-out. Furthermore, $\psi_d(\mathbf{r}_1, \mathbf{r}_2)$ denotes the deuteron

wave function. The absence of time variable in this formula does not mean that we neglect the dynamical properties. It takes into account a finite duration of the emission process as the particles are emitted simultaneously.

For the emission regions for (anti)deuterons, the nucleon source is distributed over the whole fireball, while the antinucleons are suppressed towards the center of the fireball, leading to a surface type emission for these antinucleons. The nucleon source function $\mathcal{D}(\mathbf{r})$ is parametrized by a normalized Gaussian,

$$\mathcal{D}(\mathbf{r}) = \frac{1}{(2\pi)^{3/2}r_0^3} \exp\left(-\mathbf{r}^2/2r_0^2\right) , \tag{3.14}$$

with r_0 giving the mean radius squared $\langle r^2 \rangle = 3r_0^2$. The normalized antinucleon source function $\bar{\mathcal{D}}(\mathbf{r})$ contains a second Gaussian of width r_* that effectively cuts out the central region

$$\bar{\mathcal{D}}(\mathbf{r}) = \begin{cases} \frac{1}{(2\pi)^{3/2}(r_0^3 - r_*^3)} \left[\exp\left(-\mathbf{r}^2/2r_0^2\right) - \exp\left(-\mathbf{r}^2/2r_*^2\right)\right] & \text{for } r_* \neq r_0, \\ \frac{1}{3(2\pi)^{3/2}} \frac{\mathbf{r}^2}{r_*^5} \exp\left(-\mathbf{r}^2/2r_*^2\right) & \text{for } r_* = r_0, \end{cases} \tag{3.15}$$

where r_* measures the zone where the emission of antinucleons is strongly depleted.

The integral in eq. (3.13) can be formulated using center-of-mass coordinates $\mathbf{P} = \mathbf{p}_1 + \mathbf{p}_2$, $\mathbf{R} = \frac{1}{2}(\mathbf{r}_1 + \mathbf{r}_2)$ and relative coordinates $\mathbf{q} = \frac{1}{2}(\mathbf{p}_1 - \mathbf{p}_2)$, $\mathbf{r} = \mathbf{r}_1 - \mathbf{r}_2$. The deuteron wave function then reads

$$\psi_d(\mathbf{r}_1, \mathbf{r}_2) = e^{i\mathbf{P}\cdot\mathbf{R}}\phi_d(\mathbf{r}) , \tag{3.16}$$

with the Hulthén wave function,

$$\phi_d(\mathbf{r}) = \left(\frac{\alpha\beta(\alpha+\beta)}{2\pi(\alpha-\beta)^2}\right)^{1/2} \frac{e^{-\alpha\mathbf{r}} - e^{-\beta\mathbf{r}}}{\mathbf{r}} , \tag{3.17}$$

where $\alpha = 0.23$ fm^{-1} and $\beta = 1.61$ fm^{-1} (Hodgson, 1971). For the formation rate $\mathcal{A}$ in relative coordinates, we obtain

$$\mathcal{A} \equiv \frac{3}{4}(2\pi)^3 \int d^3r \mathcal{D}_r(\mathbf{r})|\phi_d(\mathbf{r})|^2 , \tag{3.18}$$

and the nucleon source function becomes

$$\mathcal{D}_r(\mathbf{r}) = \frac{1}{(4\pi)^{3/2}r_0^3} \exp\left[-\mathbf{r}^2/4r_0^2\right] . \tag{3.19}$$

and the antinucleon source function for $r_0 = r_*$ reads,

$$\bar{\mathcal{D}}_r(\mathbf{r}) = 4\pi \left(\frac{1}{3(2\pi)^{3/2}r_*^5}\right)^2 \left[\frac{15\sqrt{\pi}}{16}r_*^7 + \frac{6\sqrt{\pi}\mathbf{r}^2}{16}r_*^5 + \frac{\sqrt{\pi}\mathbf{r}^4}{64}r_*^3\right] \exp\left(-\frac{\mathbf{r}^2}{2r_*^2}\right) . \tag{3.20}$$

and for $r_0 \neq r_*$,

$$\begin{aligned}
\bar{\mathcal{D}}_r(\mathbf{r}) =& \frac{1}{(4\pi)^{\frac{3}{2}}(r_0^3 - r_*^3)^2} \left[r_0^3 \exp\left(-\frac{\mathbf{r}^2}{4r_0^2}\right) + r_*^3 \exp\left(-\frac{\mathbf{r}^2}{4r_*^2}\right)\right. \\
&\left. - \frac{2^{\frac{5}{2}}r_0^3 r_*^3}{(r_0^2+r_*^2)^{\frac{3}{2}}} \exp\left(-\frac{\mathbf{r}^2}{2(r_0^2 + r_*^2)}\right)\right] .
\end{aligned} \tag{3.21}$$

Then the formation rate is directly proportional to the coalescence parameter B_2, which can be measured in heavy-ion experiments or obtained from transport or coalescence models, as

$$\mathcal{A} \equiv \frac{m_N \sigma^{inel}}{2} B_2 , \tag{3.22}$$

where m_N is the nucleon mass. We hereby neglect the mass difference between protons and neutrons. Note that B_2 here has a unit of GeV^2/mb which is an old formalism. In this thesis, we use the modern unit of B_2 which is GeV^2/c^2 or GeV^2 in natural units. The formation rates giving by experimental cross sections of antideuterons and antiprotons in Si-Au collisions at AGS in (Aoki et al., 1992) are

$$\mathcal{A} = 0.90 \text{ fm}^{-3}, \qquad \bar{\mathcal{A}} = 0.15 \text{ fm}^{-3},$$

By comparing above values of formation rates with the eq. (3.18), it was reported that $\langle r^2 \rangle^{1/2} = \sqrt{3}r_0 \simeq 2.5$ fm for nucleon source, where $\langle r^2 \rangle^{1/2} = 4.3$ fm for antinucleon's. This substantially means the baryon density is indeed 5 times smaller in the antinucleon source. The antideuteron formation rate is also reproduced with $r_0 \simeq r_* \simeq 1.5$ fm. In this case, the antinucleon source has the same size as the nucleon one but antinucleons are produced purely on the surface. Thus the antideuteron formation rates observed in (Aoki et al., 1992) have been explained.

This model, however, is incomplete for various reasons. We found minor mistakes in the calculation. Firstly, the relative antinucleon source function lost the coupling term of r_0 and r_*. This means that the antideuteron formation rate will be reproduced at different source shapes. Furthermore, the interpretation of the r_0 and r_* here is unclear and somehow unphysical. Antinucleons and nucleons should be produced from the whole fireball. Thus in this work, we correct the model and provide a new the interpretation for r_0 and r_*. Then, we further the idea to study the energy dependence of the emission sources.
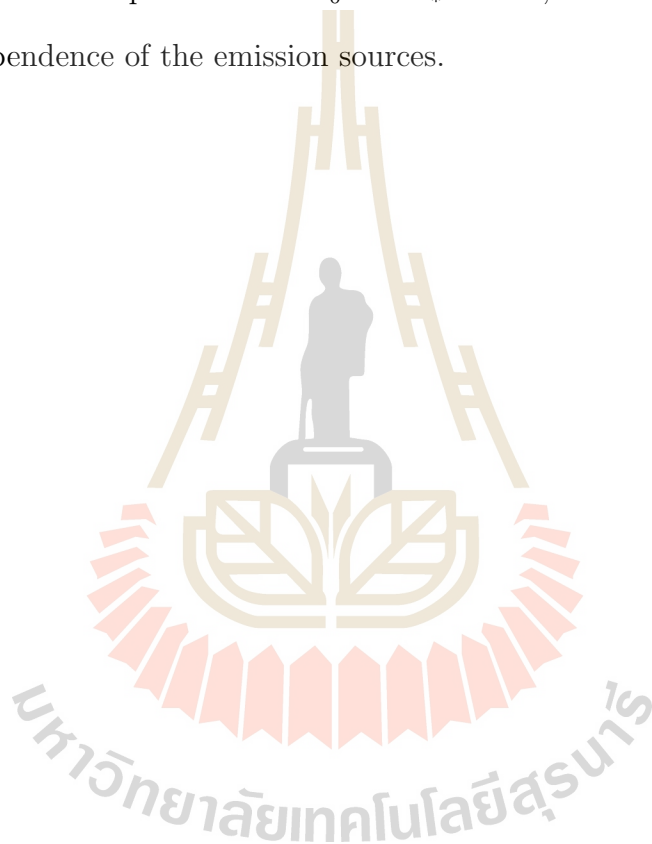
CHAPTER IV

MODEL DESCRIPTIONS

4.1 Non-Suppressed Nucleon Source

We employ the spatial coalescence approach formulated by Mrówczyński (Mrówczyński, 1993). The particle source is created when the two nuclei collide with each other and undergo a freeze-out process. The created medium contains nucleons only for low $\sqrt{s_{NN}}$ from the projectile and target nucleus. The schematic of our chosen coalescence model is presented in figure 4.1. While nucleons are emitted from the whole fireball volume. the antinucleons are emitted only from the outer shell. These pictures are similar to ones from the previous section. However the boundaries of the antinucleon and nucleon sources are defined clearly, such that they share the same fireball radius with the suppression region inside for the antideuteron source. The production cross sections for deuterons and nucleons are denoted by σ_d and σ_p. In a Lorentz invariant form, they are related by

$$E\frac{d^3\sigma_d}{d\mathbf{P}^3} = B_2\left(\frac{E}{2}\frac{d^3\sigma_p}{d\left(\mathbf{P}/2\right)^3}\right)^2 ,$$
(4.1)

where E and $E/2$ denote the deuteron and nucleon energies, respectively. B_2 is the coalescence parameter which can be measured in heavy-ion experiments or obtained from transport or coalescence models. It is directly proportional to the formation rate,

$$\mathcal{A}(r_0, r_*) \equiv \frac{m}{2}B_2(\sqrt{s_{NN}}) ,$$
(4.2)

(a) Nucleon Source   (b) Antinucleon Source
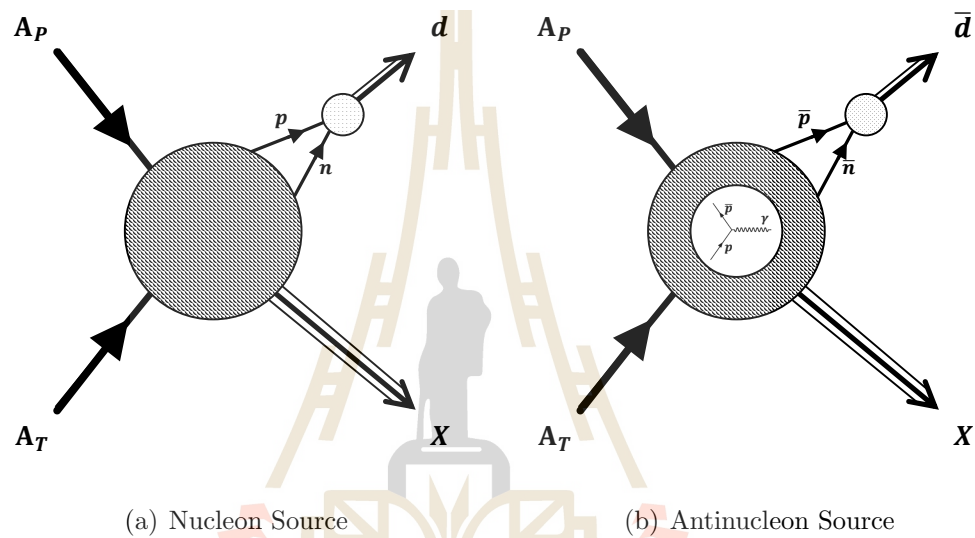
Figure 4.1 The schematics for the nucleon and antinucleon source. A_P and A_T represent the projectile and target nuclei. p, n, d and X are proton , neutron, deuteron and the rest momenta of the system. (a) Nucleons are being produced and emitted directly from the fireball and coalesce into deuterons. (b) Antinucleons suffer the $N\bar{N}$-annihilation at the central region, called the suppression region. The survived antinucleons on the outer shell coalesce into antideuterons.

where m is the nucleon mass. We hereby neglect the mass difference between protons and neutrons. The formation rate $\mathcal{A}$ in relative coordinates reads,

$$\mathcal{A}(r_0, r_*) \equiv \frac{3}{4}(2\pi)^3 \int d^3 r \mathcal{D}_r(\mathbf{r}, r_0)|\psi_d(\mathbf{r})|^2 \tag{4.3}$$

where $\psi_d(\mathbf{r})$ is deuteron wave function in Hulthén form from eq. (3.17). For the emission regions for (anti)deuterons we follow the Gaussian ansatz (Mrówczyński, 1993): The nucleon source is distributed over the whole fireball, while antinucleons are suppressed towards the center of the fireball, leading to a surface type emission for antinucleons.

$$\mathcal{D}_r(\mathbf{r}, r_0) = \frac{1}{(4\pi)^{3/2}r_0^3} \exp\left[-\mathbf{r}^2/4r_0^2\right] . \tag{4.4}$$

with the nucleon source radius r_0 which is equivalent to the fireball radius. For the antideuteron formation rate, our source functions differ from eq. (3.15) which does not contain the mixed term of r_0 and r_*. The antinucleon source function here reads

$$\bar{\mathcal{D}}_r(\mathbf{r}, r_0, r_*) = \begin{cases} \dfrac{r_0^3 e^{-\mathbf{r}^2/4r_0^2} + r_*^3 e^{-\mathbf{r}^2/4r_*^2} - \left(\dfrac{2^{5/2}r_0^3 r_*^3}{(r_0^2 + r_*^2)^{3/2}}\right) e^{-\mathbf{r}^2/2(r_0^2+r_*^2)}}{(4\pi)^{3/2}(r_0^3 - r_*^3)^2} & \text{for } r_* \neq r_0 \\[4mm] \dfrac{1}{18\pi^{3/2}}\left[\dfrac{15}{16}\dfrac{\mathbf{r}^4}{r_*^7} + \dfrac{3}{16}\dfrac{\mathbf{r}^2}{r_*^5} + \dfrac{1}{64}\dfrac{1}{r_*^3}\right] e^{-\mathbf{r}^2/2r_*^2} & \text{for } r_* = r_0 \end{cases} . \tag{4.5}$$

Figure 4.2 shows the antideuteron formation rate according to eq. (4.3) for different values of r_0 and r_*. We excluded the nonphysical region where $r_* > r_0$. The formation rate of deuterons and antideuterons are equivalent where the annihilation region disappears, i.e. at $r_* = 0$ fm. For $r_* > 0$ fm, the maximum of the antideuteron formation rate is smaller, the larger the suppression region r_* and the larger the fireball radius r_0 is.

To evaluate the source geometries via r_0 and r_*, we fit the formation rates to the experimental data obtained at different energies. Data on the coalescence
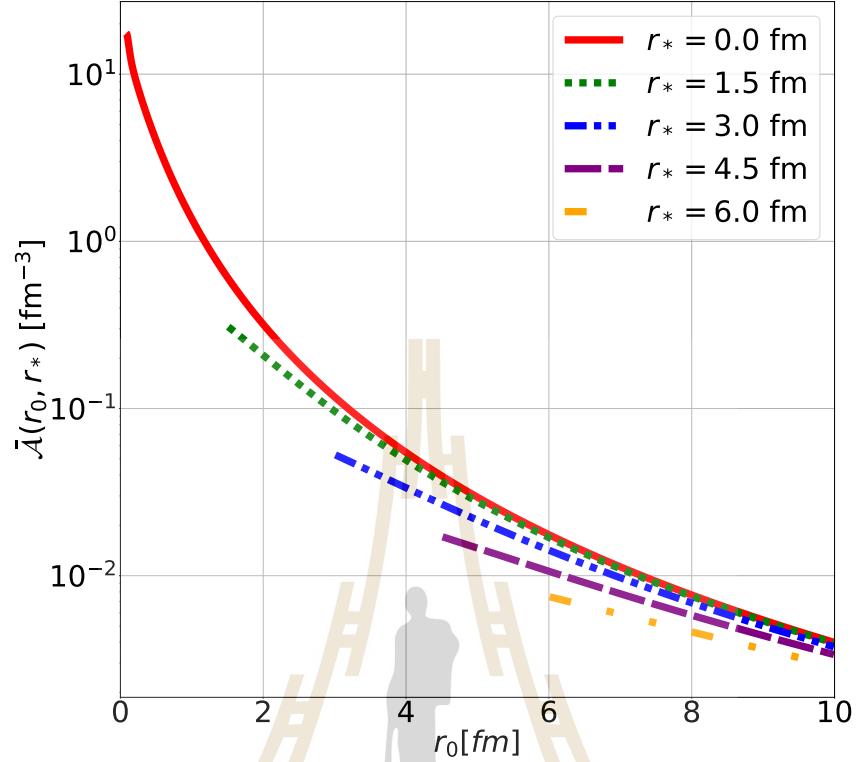
Figure 4.2 (Color line) Antideuteron formation rate as a function of the source radius r_0 as obtained from the coalescence model for several values of the suppression radius r_*.

parameter B_2 (Kabana et al., 1998; Van Buren et al., 1999; Armstrong et al., 2000; Adam et al., 2019) is shown in figure 4.3. We use these to extract the nucleon r_0 from the deuteron formation rate $\mathcal{A}$ using eq. (4.3). The NA49 data and the RHIC-BES data will be used in our calculation represented as black lines in figure 4.3. To obtain the values for the antinucleon freeze-out distribution, we assume that the total source size (parametrized by r_0 of the nucleons) stays the same and we only need to fit r_* to describe the antideuteron formation. Each experimental data point $\bar{B}_2$ is converted and compared with our calculated formation rate to extract the (r_0, r_*) conditions. The numerical implementations as well as the geometry results will be presented in the following section.
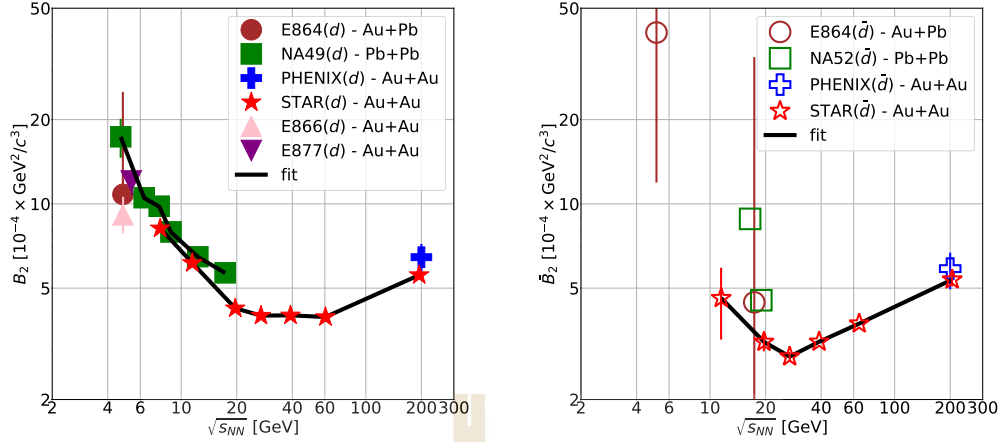
Figure 4.3 The coalescence parameters for deuterons (left) and antideuterons (right) extracted from various experimental data (Kabana et al., 1998; Van Buren et al., 1999; Armstrong et al., 2000; Adam et al., 2019) as a function of energy. The black lines shows our fit of B_2 and $\bar{B}_2$ using the extracted radii r_0 and r_* according to the Mrówczyński coalescence model (Mrówczyński, 1993).

The results for r_0 and r_* are shown in figure 4.4. At low energies, $\sqrt{s_{NN}} \leq$ 10 GeV, the fireball radius r_0 grows rapidly with center-of-mass energy and NA49 data smoothly overlaps with STAR data. A maximum value of $r_0 = 5.35$ fm is reached around $\sqrt{s_{NN}} = 63$ GeV. Toward the higher energy of 200 GeV, r_0 decreases again. This decrease is contrary to the assumption that the fireball radius increases with energy. Since the QGP phase is prominent at this energy, flow effects could significantly affect B_2. This analysis, however, beyond the scope of our model. The absolute value of the inner radius of the antideuteron production region shows an increase until $\sqrt{s_{NN}} = 27$ GeV, before depleting. Consequently, with increasing beam energy beyond 27 GeV, antinucleons have a higher probability to survive after being produced closer to the center of the fireball. This indicates that towards higher collision energies annihilation becomes less frequent when the system is no longer nucleon-, but pion-dominated.
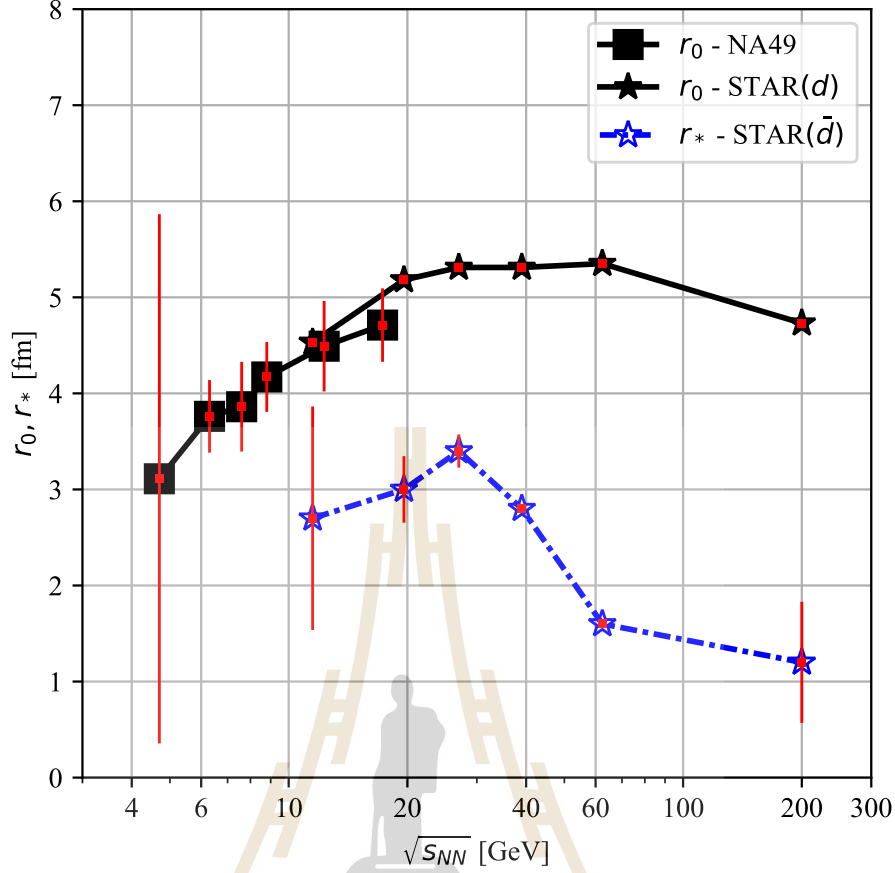
Figure 4.4 The radii r_0 and r_* as a function of energy extracted via the coalescence model. The black lines and blue dashed lines indicate the fireball radius r_0 and suppression radius r_*. The squared-symbol and star-symbol represents the data from NA49 and STAR experiments.

4.2 Charge Volume Constraint

The result from figure 4.4 shows that the fireball volume depletes at higher energy. One cannot overlook the fact that the number of charged particles N_{ch} always increases with $\sqrt{s_{NN}}$. N_{ch} is usually used as a gauge for the fireball radius/volume, i.e. $V_{ch} \propto N_{ch}^{1/3}$ (see figure 4.5).

Data from Au+Au collisions at $0-6\%$ centrality at PHENIX shows continuous increase of the number of charged particles or the charged volume with $\sqrt{s_{NN}}$ seems to contradict our result as we go toward higher energies, where r_0 or source volume
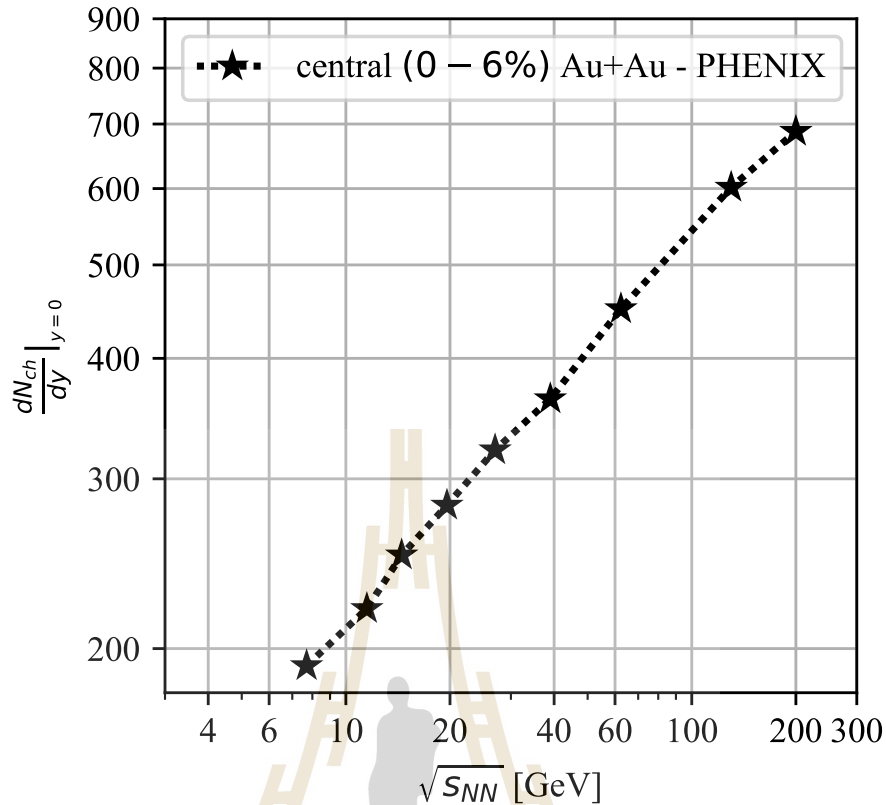
Figure 4.5 The number of charged particle at mid-rapidity as a function of center-of-mass energy from PHENIX (Adare et al., 2016).

drops down instead. There is a way to account for these problems. We can slightly change the interpretation of the charged volume fireball into the RMS-radius of the (anti)nucleon source or fireball instead. While the RMS radius is constrained to the number of charged particles N_{ch}, the fireball radius r_0 and suppression radius r_* are not affected directly, thus they can still keep variable features.

At first, we came up with three simple approaches:

- Non-suppressed nucleon source - assumes a shared fireball of nucleons and antinucleons. Nucleons are in a bulk type and antinucleons are in a shell type.

- Shared fireball - assumes a shared fireball but both sources are described as a shell type.

- Separated fireballs - assumes both sources are unique and independent of each

other.

Although the first choice, non-suppression nucleon source, sounds reasonable since we want to compare this charged constraint method to the previous Mrówczyński coalescence model (bulk nucleon source). We found that this approach leads to infinite possibilities of antinucleons geometries. The reason lies in the choice of proportionality factor between the number of charged particles and the RMS radius since we have no clear analytical value for that. The second choice, the shared fireball model, could also maintain the interpretation where nucleons and antinucleons share the same fireball r_0 and both sources have a shell-like structure. However, this case raises another problem in which r_0 determines the real fireball size?, since both sources are shell types and carrying their own fireball r_0 and suppression radius r_*. So this approach needs more work and exceeds the scope of our studies. In this thesis we will investigate the independent (anti)nucleon source geometries meaning that both RMS-radii of (anti)nucleon sources are constrained and their geometries are allowed to have their own fireball r_0 and suppression radius r_* independently. With this method, we can avoid the bias on whether or not the nucleon source has a suppression. In addition, the proportionality factor can be dealt with easily.

We put a constraint into the $\sqrt{\langle \mathbf{r}^2 \rangle}$ or root-mean-squared radius (RMS) of previous source function by the number of charged particles. $\sqrt{\langle \mathbf{r}^2 \rangle}_{source}$ is derived from the square root of $\int_0^\infty \mathbf{r}^2 \bar{D}(\mathbf{r}, r_0, r_*) d\mathbf{r}$ for the antinucleon source. Note that r_* is equal to zero for the nucleon source.

$$\sqrt{\langle \mathbf{r}^2 \rangle} = \begin{cases} \sqrt{\dfrac{5}{3}} r_0 & \text{for } r_0 = r_* \\ \sqrt{3 \left(\dfrac{r_0^5 - r_*^5}{r_0^3 - r_*^5} \right)} & \text{for } r_0 \neq r_* \end{cases}, \tag{4.6}$$

which is also conceivably equal to

$$\sqrt{\langle \mathbf{r}^2 \rangle} = const \cdot N_{ch}^{1/3} . \tag{4.7}$$

Let's recall the relation of the formation rate $\mathcal{A}$ and the coalescence parameter B_2, eq. (4.2).

$$\frac{m_N}{2}\mathcal{A}(r_0, r_*) = B_2(\sqrt{s_{NN}}) \ .$$

Now we have two equations from above with 2 unknowns to solve, i.e. r_0 and r_*. We can extract the r_0 and r_* simultaneously at each energy $\sqrt{s_{NN}}$ by finding the root of eq. (4.2) & (4.7) as shown in figure 4.6

According to the B_2 data provided by STAR(d), we can study the nucleon source geometry for $\sqrt{s_{NN}} = 7.7 - 200$ GeV. For antinucleons, the energy provided by STAR($\bar{d}$) ranges from $\sqrt{s_{NN}} = 11.5 - 200$ GeV (Adam et al., 2019). Here, the constant value for the proportionality between $\langle \mathbf{r}^2 \rangle^{1/2}$ and $N_{ch}^{1/3}$ is found to be 0.925.

The crossing points between formation rate $\mathcal{A}$ and the RMS-radius $\langle \mathbf{r}^2 \rangle^{1/2}$ determine the (anti)nucleon source geometries and are shown in figure 4.7. We found that both nucleon and antinucleon sources grow with energy as we expected given the constraint. Especially for $\sqrt{s_{NN}} \geq 39$ GeV, both nucleon and antinucleon sources seem to be sharing the same fireball radius as we speculated earlier. The growing of the suppression region r_* agrees with the previous result (figure 4.4) where it reaches a maximum at $\sqrt{s_{NN}} = 27$ GeV. Furthermore, as the energy increases, both source radii rapidly decrease. The reasoning for this is similar to our former statement of the pion enhancement in section 4.1. At higher energy, pions dominate the fireball and suppress nucleon-antinucleon annihilation. However, the drop of r_* of nucleons to zero at $\sqrt{s_{NN}} = 200$ GeV means that the pion domination does not directly suppress the nucleon source.
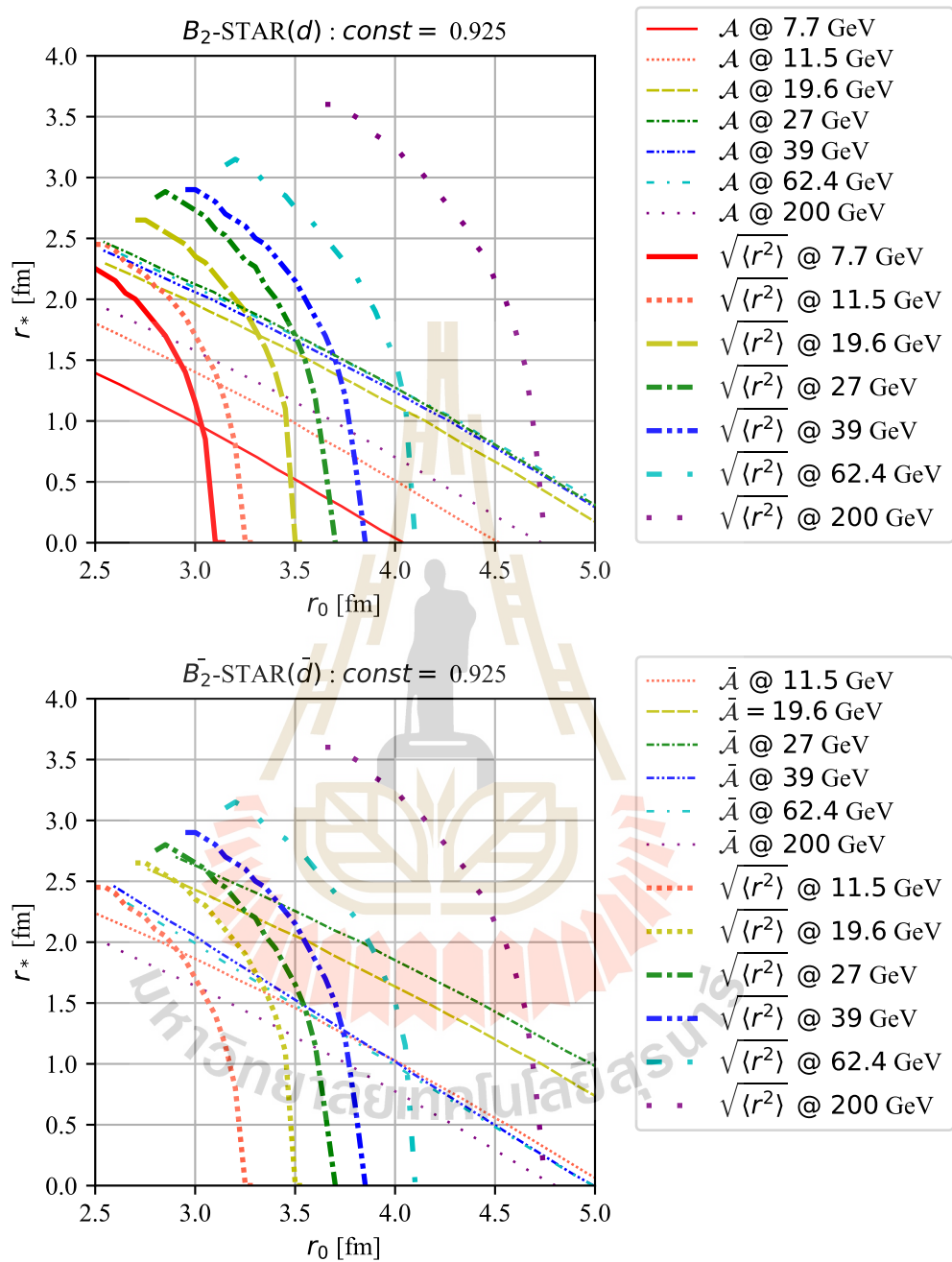
Figure 4.6 The (anti)deuteron formation rate $\mathcal{A}(r_0, r_*)$ from $\text{STAR}(d)$ and $\text{STAR}(\bar{d})$ and the RMS-radius of (anti)nucleon source in the (r_0, r_*) space from PHENIX. The solid-line represents one satisfied the formation rate function. The dotted-line is the (r_0, r_*) satisfied the RMS-radius function.
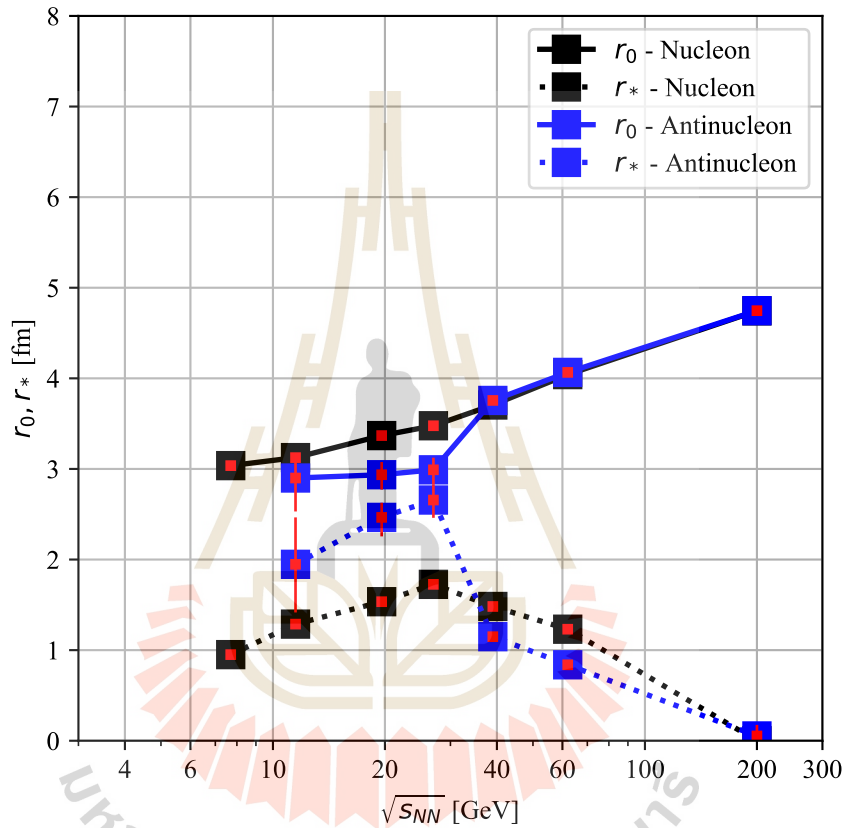
Figure 4.7 The (anti)nucleon source geometry plot with a function of energy $\sqrt{s_{NN}}$. The solid-line and dashed-line indicate the fireball radius and suppression radius respectively. The black and blue color differentiate between nucleon and antinucleon source.

CHAPTER V

NUMERICAL IMPLEMENTATION

5.1 Non-suppressed nucleon source

We start by ensuring the normalization of the source functions $\mathcal{D}_r$ and $\bar{\mathcal{D}}_r$. Then we proceed through the following steps;

- Calculate the formation rate of nucleon and antinucleon source using Simpson's integration method.

- Extract a fireball radius r_0 for both nucleon and antinucleon source using the least difference of the formation rate of nucleon between $\mathcal{A}(r_0)$ and $\mathcal{A}(\sqrt{s_{NN}})$.

- Determine the suppression region r_* from each fireball radius r_0 by comparing $\bar{\mathcal{A}}(r_0, r_*)$ with $\bar{\mathcal{A}}(\sqrt{s_{NN}})$.

5.1.1 Formation Rate Integration

The formation rate of the deuteron and antideuteron $\bar{\mathcal{A}}(r_0)$, $\mathcal{A}(r_0, r_*)$ from eq. (4.3) are calculated similarly using Simpson's rule, a method for numerical integration. The numerical approximation of definite integrals is given by,

$$\int_a^b f(x)dx \sim \frac{\Delta x}{3}\left(f(x_0) + 4f(x_1) + 2f(x_2) + 4f(x_3)\right) + ... + 4f(x_{n-1}) + f(x_n)\right),$$

(5.1)

where $\Delta x = \frac{b-a}{n}$ and $x_n = a + n\Delta x$. This can also be written as,

$$\int_a^b f(x)dx = \left(\frac{b-a}{N}\right)\frac{1}{3}\sum_{n=0}^{N} u_n f(a + n\Delta x) \begin{cases} u_n = 1, & \text{if } i = 0 \text{ or } i = N \\ u_n = 2, & \text{if } i \text{ is even} \\ u_n = 4, & \text{if } i \text{ is odd} \end{cases}, \quad (5.2)$$

where a and b are the lower and upper boundary, N is the number of intervals. This method converges faster and and is more precise than, e.g., the Trapezoid rule.

First of all, we have to check the normalization of the relative source function D_r and $\bar{D}_r$ within r_0 and (r_0, r_*) space. The (anti)deuteron formation rate is spherically symmetric. We can reduce the dimensions of integration from 3D spherical into radial 1 dimension. The volume element becomes then $4\pi r^2 dr$. The numerical expression of the deuteron formation rate for each r_{0_j} is,

$$\mathcal{A}(r_{0_j}) = \int_{a=0}^{b=10} D_r(r, r_{0_j})|\phi(r)|^2 4\pi r^2 dr$$
$$= \left(\frac{10-0}{50}\right)\frac{1}{3}\sum_{i=0}^{N=50} u_n \left[D_r\left(0 + n0.2, r_{0_j}\right)\left|\phi\left(0 + n0.2\right)\right|^2 4\pi\left(0 + n0.2\right)^2\right]$$
$$(5.3)$$

Since the data is mostly based on Au+Au $0 - 10\%$ central collisions at low- to mid-energy, the fireball radius should not exceed that of the gold radius, i.e., ~ 7 fm. So the upper boundary limit of 10 fm is reasonable. With $a = 0$ fm, $b = 10$ fm and $N = 50$, we set the spacing of the Δr to be 0.2 fm. This resolution has been optimized and gives a satisfying convergence behavior. The results of the formation rate are plotted in figure 5.1.

Then the formation rate of antideuterons is calculated in a similar way but the formation rate $\bar{\mathcal{A}}$ will be in (r_0, r_*) space. The numerical expressions for (r_{0_j}, r_{*_k}) read,
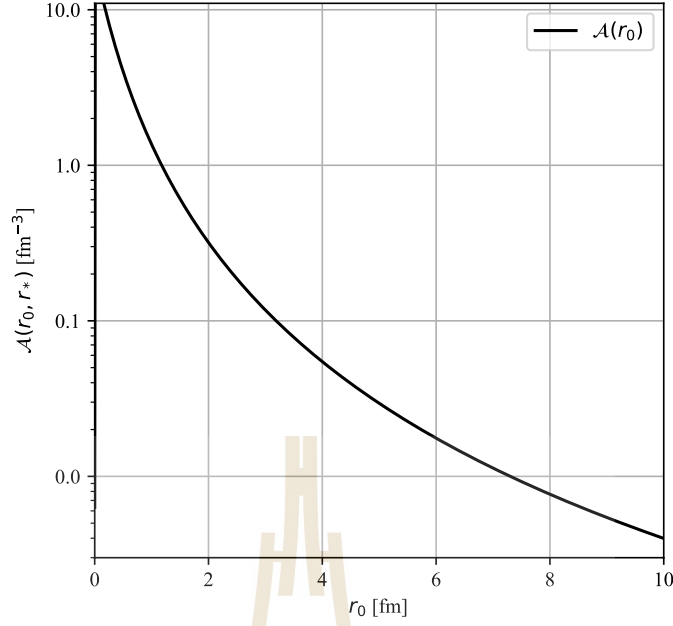
Figure 5.1 The deuteron formation rate in r_0 space.

for $r_{0_j} \neq r_{*_k}$:

$$\bar{\mathcal{A}}(r_{0_j}, r_{*_k}) = \int_{a=0}^{b=10} \bar{\mathcal{D}}_r(r, r_{0_j}, r_{*_k})|\phi(r)|^2 4\pi r^2 dr$$

$$= \left(\frac{10-0}{50}\right)\frac{1}{3}\sum_{i=0}^{N=50} u_n \left\{ \left[r_{0_j}^3 e^{-\frac{(0+n0.2)^2}{4r_{0_j}^2}} + r_{*_k}^3 e^{-\frac{(0+n0.2)^2}{4r_{*_k}^2}} - \frac{2^{\frac{5}{2}} r_{0_j}^3 r_{*_k}^3}{(r_{0_j}^2 + r_{*_k}^2)^{\frac{3}{2}}} e^{-\frac{(0+n0.2)^2}{2\left(r_{0_j}^2 + r_{*_k}^2\right)}} \right] \right.$$

$$\left. \times \left(\frac{1}{(4\pi)^{\frac{3}{2}} (r_{0_j}^3 - r_{*_k}^3)^2} \right) \left[\left|\phi\left(0+n0.2\right)\right|^2 4\pi\left(0+n0.2\right)^2 \right] \right\} .$$

(5.4)

for $r_{0_j} = r_{*_k}$:

$$\bar{\mathcal{A}}(r_{0_j}, r_{*_k}) = \int_{a=0}^{b=10} \bar{\mathcal{D}}_r(r, r_{0_j}, r_{*_k})|\phi(r)|^2 4\pi r^2 dr$$

$$= \left(\frac{10-0}{50}\right)\frac{1}{3}\sum_{i=0}^{N=50} u_n \left\{ \left[\frac{15}{16} r_{*_k}^7 + \frac{6(0+n0.2)^2}{16} r_{*_k}^5 + \frac{(0+n0.2)^4}{64} r_{*_k}^3 \right] \right.$$

$$\left. \times 4\pi \left(\frac{1}{3(2\pi)^{3/2} r_{*_k}^5} \right)^2 e^{-\frac{(0+n0.2)^2}{2r_{*_k}^2}} \left|\phi\left(0+n0.2\right)\right|^2 4\pi\left(0+n0.2\right)^2 \right\} .$$

(5.5)

The result gives a 2D-array of antideuteron formation rates in 2 coordinates, i.e., r_0 and r_*. The result of the integral is plotted and shown in figure 5.2. Recall
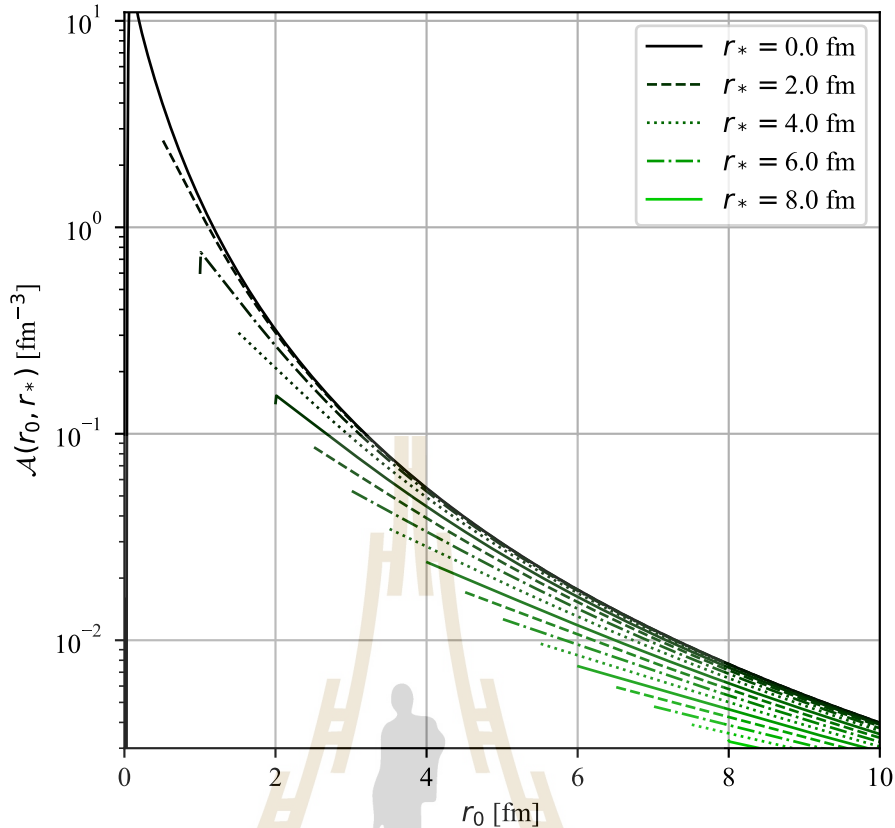
Figure 5.2 The antideuteron formation rate in r_0 space for different r_*. The smaller r_* gives the upper limit to the antideuteron formation rate in r_0 space. Note that the area of $r_0 < r_*$ is undefined. So it is excluded from the calculation.

that, we use $r_0 - \text{step} = 0.01$ fm for each r_{0_j} for the deuteron formation rate. Now, we set the $r_* - \text{step}$ to 0.1 fm for each r_{*_k} starting from $0 - 10$ fm. As we will see later, the formation rate is more sensitive to the r_0 than r_*. The change of r_0 strongly affects the antideuteron formation rate. Thus we don't need much refined r_* scale.

5.1.2 Nucleon Source Radius r_0 Extraction

Now that we have calculated all possible value of the deuteron formation rate $\mathcal{A}(r_0)$ as shown in figure 5.1, we will scan through all possible values r_0 and compare the corresponding formation rate $\mathcal{A}(r_0)$ with the experimental value $\mathcal{A}(\sqrt{s_{NN}})$.

We start by converting the coalescence parameter at i^{th} energy B_{2_i} into the

formation rate at i^{th} $\mathcal{A}_i$ according to eq. (4.2),

$$\mathcal{A}_i = \frac{m_N}{2} B_{2_i} \left(\frac{1}{197} \ [\text{MeV} \cdot \text{fm}] \right)^3.$$ (5.6)

The extra parenthesis suitably transforms unit of the right-hand side $[\text{MeV}]^3$ into $[\text{fm}]^{-3}$, the unit of the formation rate. As mentioned before, we neglect the mass difference of proton and neutron and just use the nucleon mass $m_N = 0.94$ MeV. The available B_2 data for $\sqrt{s_{NN}}$ =4.7, 6.3, 7.7, 8.8, 12.3, 17.3 GeV and 7.7, 11.5, 19.6, 27, 39, 62.4, and 200 GeV provided by NA49 and STAR experiments is shown in figure 5.3 to extract the fireball radius r_0.

The differently colored plus-symbols indicate the different matching points of each energy. The fireball radius of the nucleon source can be easily extracted by mapping the corresponding r_0 to each formation rate per energy. However, numerically, we cannot find the exact intersection point. We employ the absolute least-difference method between the converted formation rate $\mathcal{A}(\sqrt{s_{NN}})$, eq. (5.6) and the integrated formation rate $\mathcal{A}(r_0)$, eq. (5.3). We start by calculating their differences at i^{th} energy,

$$\left| \mathcal{A}(r_{0_j}) - \mathcal{A}(\sqrt{s_{NN_i}}) \right| = Dif_j$$ (5.7)

Dif_j is the difference per r_{0_j} step. Once we iterate until we collect all j^{th} steps, we then extract an index j of the minimum value from the Dif-array. Finally, we generate the r_{0_i} using the extracted index. Thus acquire the fireball radius r_0 at i^{th} energy.

5.1.3 Antinucleon Source Radius r_* Extraction

We assume that nucleons and antinucleons share the same fireball. In the last section we have shown how to extract the fireball r_0 at difference energies. Thus we have only the extracting of suppression radius r_* left to work on in this section. Again, we perform the least difference method between the integrated antideuteron
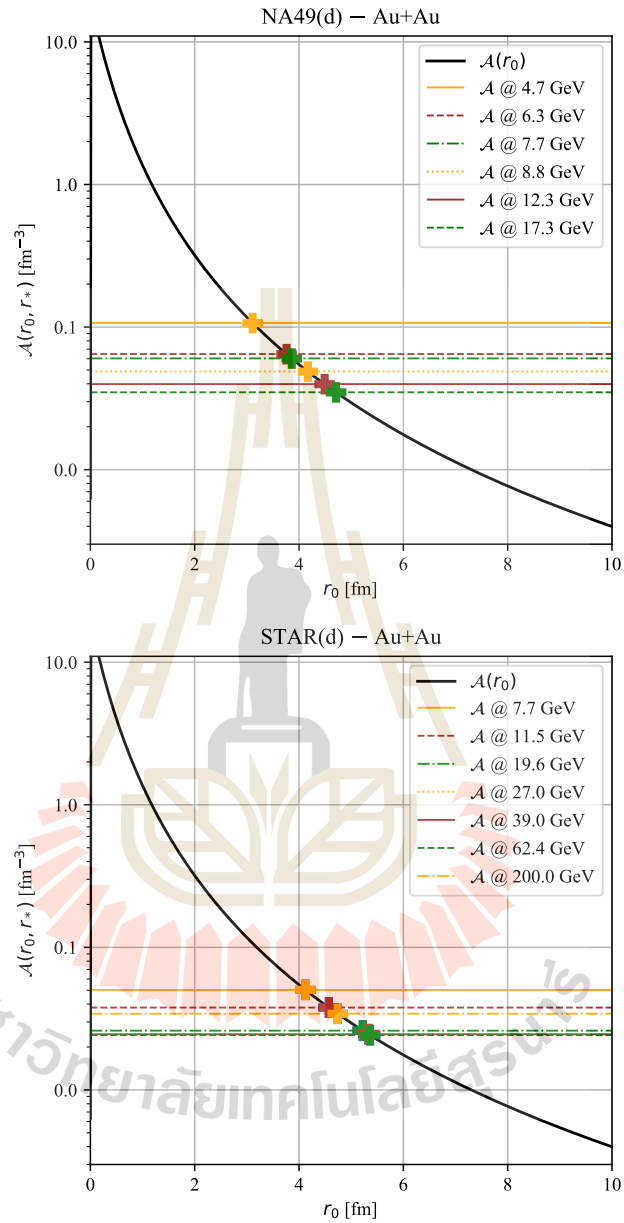
Figure 5.3 The converted formation rate from experiment is represented by horizontal lines. The crossing points indicate the fireball r_0 of the nucleon source. (Top) The formation rate from NA49 experiment. (Bottom) The formation rate from STAR experiment.
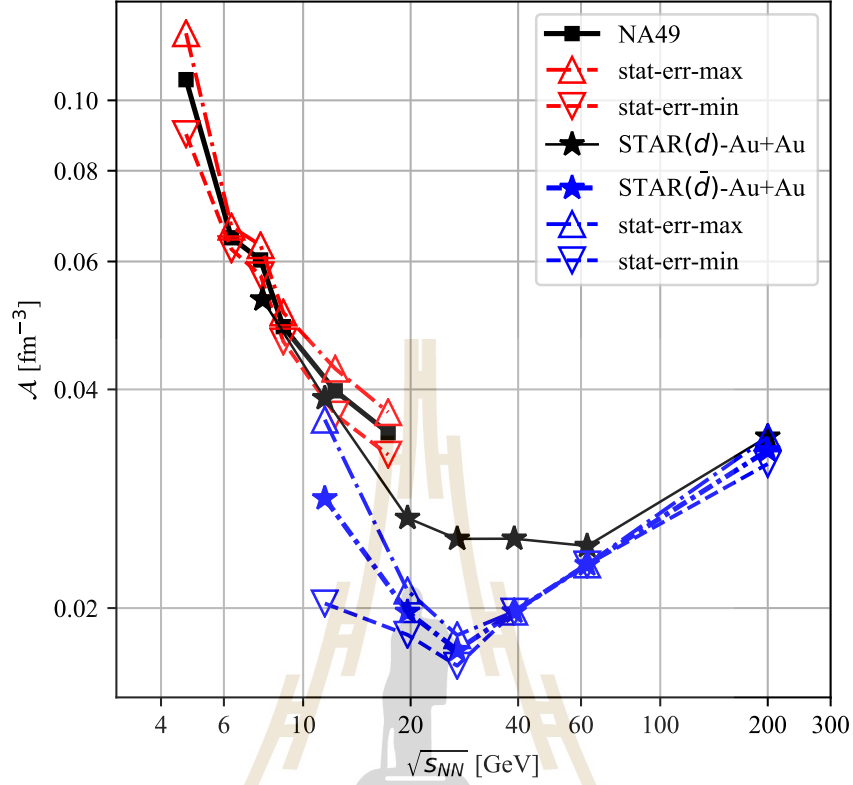
Figure 5.4 The (anti)deuteron formation rate converted from the coalescence parameters B_2.

formation rate $\mathcal{A}(r_0, r_*)$, eq. (5.4) and the converted antideuteron formation rate $\bar{\mathcal{A}}(\sqrt{s_{NN}})$, eq. (5.6),

$$\left|\bar{\mathcal{A}}(r_{0_i}, r_{*_k}) - \bar{\mathcal{A}}(\sqrt{s_{NN_i}})\right| = Dif_k \tag{5.8}$$

Notice that the fireball radius r_0 is now carrying the same i-index as the energy. This is because we input the extracted fireball radius r_0 at i^{th} from the previous section instead of generated r_0-array with j-steps. Finally, the index of minimum value from Dif-array will generate the suppression radius r_{*_i} for i^{th} energy.

5.1.4 Propagation of Error

The available data of coalescence parameters B_2 contain the experimental errors. However, only NA49 and $\text{STAR}(\bar{d})$ provide proper error bars. In this thesis, we neglect the systematic errors and focus only on the statistical error and its propagation. For simplicity, we propagate the error numerically. The provided maximum and the minimum of the coalescence parameters, i.e., $B_{2,\text{max}}$ and $B_{2,\text{min}}$ are used in the conversion, resulting in the minimum and the maximum limit of the (anti)deuteron formation rate as shown in figure 5.4. The up and down triangle-symbol indicate the upper and lower limits of the formation rate. The upper limit of the coalescence parameter corresponds to the upper limit of the formation rate. Then we follow the eq. (5.3) & (5.4) respectively to extract $r_{0,\text{max}}$ and $r_{*,\text{max}}$ and $r_{0,\text{min}}$ and $r_{*,\text{min}}$ according to the formation rate at each energy. The results in figure 5.5 give the upper limit and lower limit to the fireball and suppression radius. At lower energy, both fireball and suppression radius can fluctuate very strongly because experimental data of B_2 have a very large statistical error bars.

5.2 Charge Volume Constraint

Nucleon source and antinucleon source geometries are extracted with the same ways by the following processes,

- Find all possible roots of (r_0, r_*) pairs which satisfy the formation rate condition, $\mathcal{A}(r_0, r_*)$

- Find all possible roots of (r_0, r_*) pairs which satisfy RMS-radius condition, $\sqrt{\langle \mathbf{r}^2 \rangle}$

- Extract the (r_0, r_*) pairs that are closest in (r_0, r_*) space.
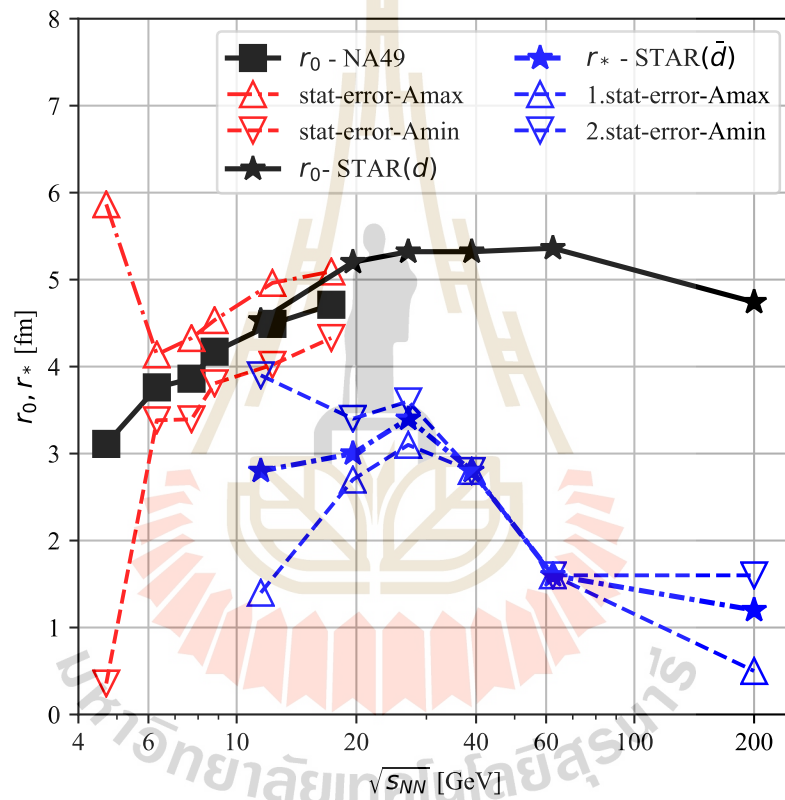
Figure 5.5 The upper limit and lower limit of the fireball radius r_0 and suppression radius r_* calculated from experiment statistical error.

5.2.1 Roots from formation rate condition

We follow that same procedure of converting formation rate and compare it with the integrated formation rate in the above section, eq. (5.8). However, we skip the step of fireball radius extraction and directly calculate the curve of the formation rate in (r_0, r_*) space.

In this approach, both nucleon and antinucleon source are parametrized as shell-like sources, i.e., $\bar{\mathcal{D}}(r_0, r_*)$. Therefore, the formation rates will have the same numerical expressions as eq. (5.4). Then we will extract all possible roots using the absolute least-difference again, $\left|\bar{\mathcal{A}}(r_{0_j}, r_{*_k}) - \bar{\mathcal{A}}(\sqrt{s_{NN_i}})\right| = Dif_m$.

Both source geometries will be extracted by exactly the same procedure. Here, we have r_0 and r_* varied from $0-10$ fm with each $j-step = 0.01$ fm and $k-step = 0.1$ fm. At the ith energy, for each r_{0_j}, we find the minimum value in Dif-array and extract the corresponding index. Here the numbers of possible differences m equals to k. So we can generate a $r_{*_{k-root}}$ and acquire a pair of $(r_{0_j}, r_{*_{k-root}})$. After we iterate the process for all possible j-step we can map a curve of eq. (5.4) in r_0 and r_* domain. Note that we must exclude the non-physical region where $r_* > r_0$.

5.2.2 Roots from RMS-radius condition

According to eq. (4.7), the RMS-radius is related to the cubic root of the number of charged particles, $N_{ch}^{1/3}$. Its numerical expression for each ith energy is,

$$\sqrt{\langle \mathbf{r}^2 \rangle}(r_{0_j}, r_{*_k}) = const \cdot N_{ch_i}^{1/3} \tag{5.9}$$

Again, we have r_0 and r_* varied from $0 - 10$ fm with each $j - step = 0.01$ fm and $k - step = 0.1$ fm. Then we use the absolute least-difference method,

$$\left| \sqrt{3\frac{(r_{0_j}^5 - r_{*_k}^5)}{(r_{0_j}^5 - r_{*_k}^5)}} - const \cdot N_{ch_i}^{1/3} \right| = Dif_m \tag{5.10}$$

(a) Nucleon source - $const = 1.0$ (b) Antinucleon source - $const = 1.0$

(c) Nucleon source - $const = 0.8$ (d) Antinucleon source - $const = 0.8$
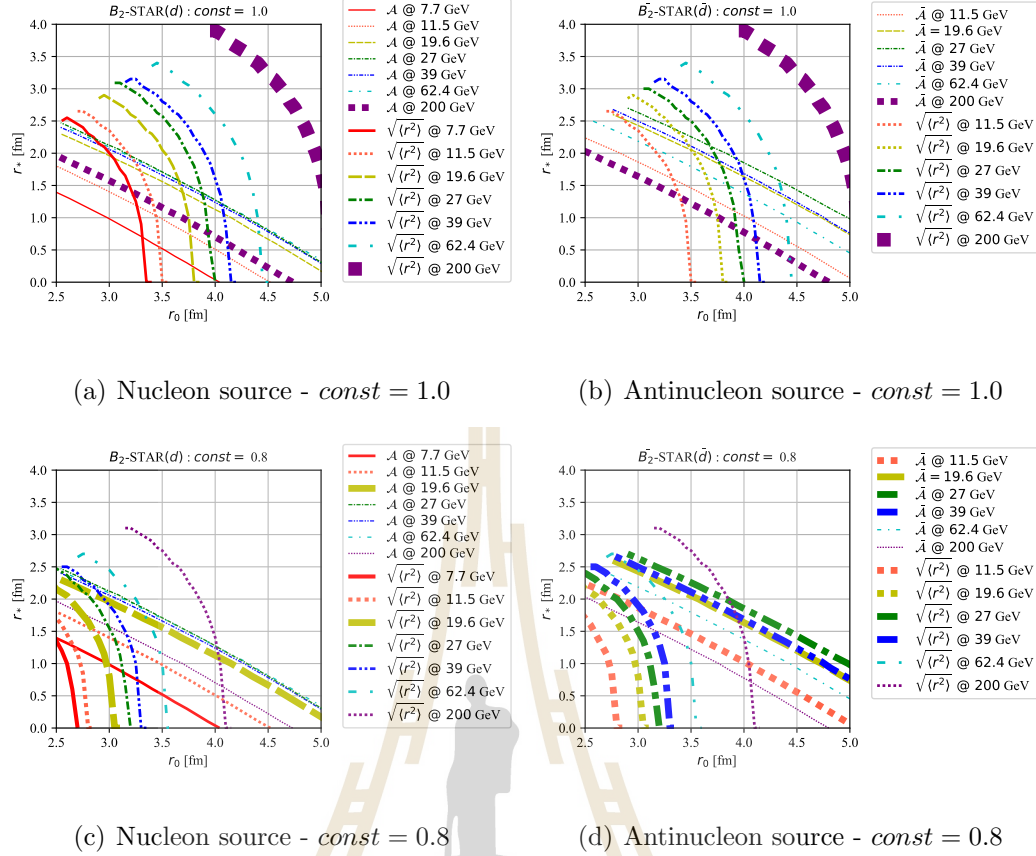
Figure 5.6 The (anti)deuteron formation rate and RMS functions with different $const$ values are plotted together in (r_0, r_*) space. The crossing points are the roots that satisfy both two equations. (a) and (b) show the consequence of using $const = 1$. (c) and (d) show the consequence of using $const = 0.8$. The colours describe a different energies

We determine the roots of (r_0, r_*) by looking at each ith energy and j^{th} r_0. The RMS radius function does not differentiate the source species as it depends only on the number of charged particles and the proportionality constant. Thus both nucleon and antinucleon source will share the same root curve in r_0 and r_* space. The constant could not be determined analytically, so we start by guessing the number and fitting.

Figure 5.6 shows the curves of (anti)deuteron formation rates and RMS functions with difference $const$ values. By using $const = 1$, we can see the crossing point from all energy ranging from $\sqrt{s_{NN}} = 7.7 - 62.4$ GeV except 200 GeV as clearly

shown in figures 5.6(a)-5.6(b). On the other hand, if we lower the *const* to 0.8, The curves of $\sqrt{\langle \mathbf{r}^2 \rangle}$ are overly shifted to the left, as you see in figures 5.6(c) and 5.6(d). The former shows the failure starting from $\sqrt{s_{NN}} = 7.7 - 27$ GeV. Although, the red curves of 7.7 GeV seem to match but numerically, they do not. This is also the case for the latter (figures 5.6(d)). The curves start to cross only after $\sqrt{s_{NN}} = 62.4$ GeV to 200 GeV. So we have to fix the constant between from $0.8 - 1.0$ such that combined two curves of eq. (5.4) and eq. (5.9) satisfy all possible conditions at different energies simultaneously. Finally, we found that the value is *const* $= 0.925$ yields a proper (anti)nucleon source geometries for all available energies (figure 4.6).
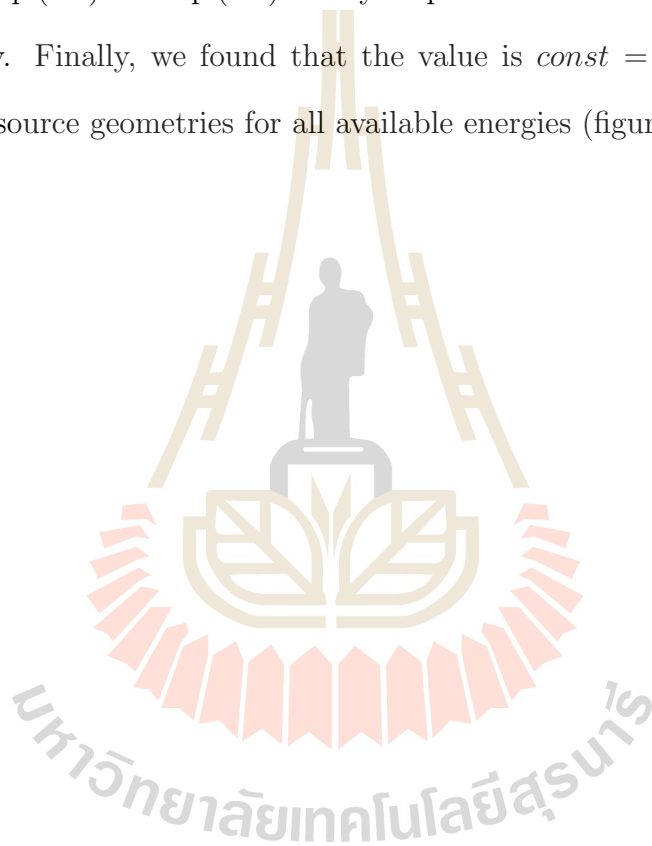
CHAPTER VI

ULTRA-RELATIVISTIC QUANTUM

MOLECULAR MODEL

The Ultra-relativistic Quantum Molecular Dynamics (UrQMD) model applies empirical potential and theoretical approximations for an effective solution of relativistic microscopic transport theory. It generates the full space-time dynamics for all included particles. The main advantages are that first, it needs no equilibration condition as thermodynamics approaches do, thus we can observe any microscopic change along the evolution process. Second, we do not need to explicitly introduce quarks and gluon degrees of freedom. Instead, we consider the strings and hadrons that are excited by the binary collisions. Here we review some general basics of the Boltzmann equation to the model implementation and briefly introduce the UrQMD initialization and the output for the simulations and calculations, for more details see ((Bass et al., 1998; Bleicher, Zabrodin, et al., 1999). Then we present our analysis approach for the source geometry using UrQMD.

6.1 Boltzmann Equation

The goal of any transport theory is to describe a relation between the streaming particles and the source (collisions terms). With the constant collision of many-body particles, it is reasonable to describe the heavy-ion collisions with the well-known Boltzmann equation,

$$p^\mu \partial_\mu f_i(x^\nu, p^\nu) = \mathcal{C}_i \tag{6.1}$$

This is a time evolution of the distribution function for particle i in phase space

$f_i(x^\nu, p^\nu)$. The source or the collisions term $\mathcal{C}_i$ is on the level of binary collisions and $2 \to n$ reactions which enable us to track along the time step. In heavy-ion collisions, the energy density is high enough to neglect the external potential on the left-hand side which is not discussed here.

6.2   UrQMD Initialization and Output

UrQMD model is designed as a multipurpose tool for studying hadron-hadron collisions, hadron-nucleus collisions, and also heavy-ion collisions. The most important part in UrQMD is including the empirical potential, such as Skyrme, Yukawa, Coulomb, and Pauli potential, instead of using QED and QCD first principle calculations. This does not mean that UrQMD neglects quantum effects for simplicity, it is also equipped with full particle-antiparticle symmetry, isospin symmetry with only flavour-SU(3) states. At high energies, the quark and gluon degrees of freedom cannot be neglected. Excitations of the string model are used for describing decay and resonance/hadron productions. All the related parameters are constantly updated and fitted to experimental data.

The projectile and the target nuclei are characterized by the Wood-Saxon profile in coordinate space and the nucleons are carrying Fermi momenta randomly distributed in the rest frame of the corresponding nucleus. The interactions of the collisions will start if the hadrons or nuclei reach the collision criteria,

$$b < \sqrt{\frac{\sigma_{\text{tot}}}{\pi}}, \tag{6.2}$$

where b is the impact parameter and σ_{tot} total cross-section corresponding to the hadrons. The σ_{tot} is energy $\sqrt{s_{NN}}$ and species i dependent. In UrQMD, there are 55 baryon and 32 meson species, ground state particles, and all resonances with their specific properties and interaction cross-sections. In addition, we can indicate the number of events and the collision time for collecting the statistical processes.

UrQMD gives us an essence of all particles of a given event at a certain time step. The information/history on all collisions, decays, produced resonances, and all stable particles are provided. These particles are described in both 3D configuration and momentum coordinates, including the energy , charge, and quantum numbers at all time-steps.

6.3 r_T Distribution

The previous two geometries in chapter IV are in agreement with the pion suppression at higher energy. However, the charged constraint model gives the impression that the pion enhancement does not directly suppress the nucleon source as the r_* of nucleon drops to zero at $\sqrt{s_{NN}} = 200$ GeV (figure 4.7). To confirm this statement, we use UrQMD to see the dynamics of (anti)nucleons and extract the freeze-out source geometries.

We simulate $0-10\%$ central Au+Au collisions at $\sqrt{s_{NN}} =$7.7, 11.5, 14.5, 19.6, 27, 39, 62.4 and 200 GeV. Then the nucleon and antinucleon distributions are studied in the transverse plane, where we assume a cylindrical geometry. The expression of the (anti)nucleon distribution is $\frac{1}{r_T}\frac{dN}{dr_T}$ where $r_T = \sqrt{r_x^2 + r_y^2}$. In figure 6.1 we show examples for the transverse distribution of (anti)nucleons as a function of r_T at $\sqrt{s_{NN}} = 11.5$ and 200 GeV.

At 11.5 GeV, $r_T < 5$ fm, nucleons are suppressed 5% below the maximum value, while the suppression of antinucleon is very strong and obvious with 80% below the maximum. On the other hand, at 200 GeV, both nucleons and antinucleons are suppressed similarly by around $60-70\%$ at the core of the sources. From this, we can say that from low to high energies, both antinucleons and nucleons always suffer from some kind of suppression. For the antinucleon case, the nucleon-antinucleon annihilation suppression is relieved by the lesser nucleon distribution at the core. The only thing that suppresses antinucleons now are pions. As you can see at 200

(a) $\sqrt{s_{NN}} = 11.5$ GeV   (b) $\sqrt{s_{NN}} = 200$ GeV
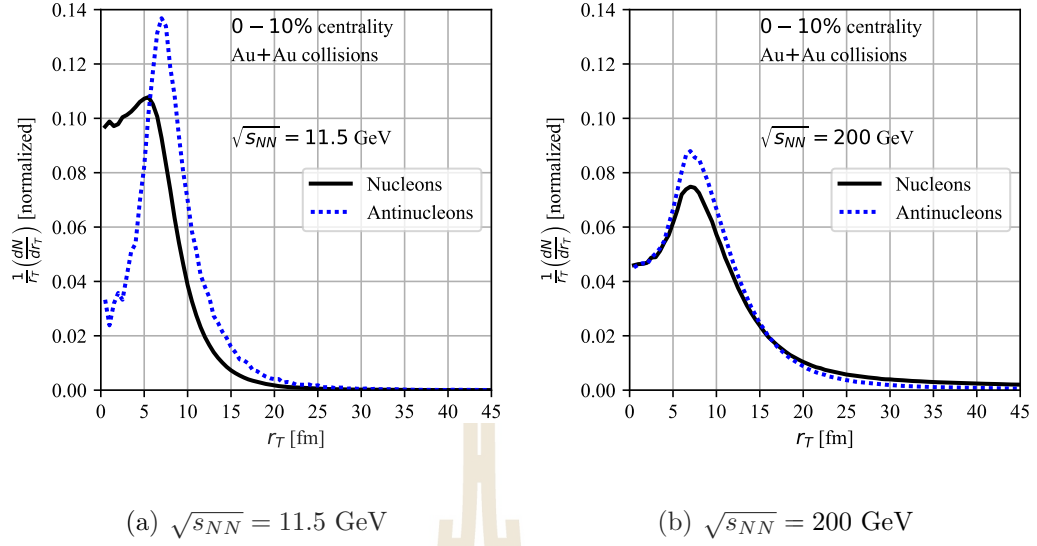
Figure 6.1 The normalised (anti)nucleon distribution in transverse plane as a function of center-of-mass energy. The solid-line and dashed-line represent the nucleon and antinucleon distributions.

GeV, the nucleon suppression is stronger at higher energy. This also comes from the fact that pions dominate the fireball and thus suppress the nucleons. Hence, the percentage of suppression between antinucleons and nucleons is roughly the same. The dynamical results contradict the charged constraint method where the suppression of (anti)nucleon r_* drops to zero at 200 GeV. However, keep in mind that in that method we do not assume the minimum suppression of nucleon source at low energy. Also if we apply the near-zero r_* of the nucleon, there will be no matching pair of (r_0, r_*) at least at 200 GeV.

After seeing the quantitative distribution of the source, we now can extract the source geometries for the physical intuition quantitatively, by fitting the (anti)nucleon distributions with source functions $\mathcal{D}(r_0)$ and $\bar{\mathcal{D}}(r_0, r_*)$ for nucleons and antinucleons respectively. We assume the simple source function from the non-suppressed nucleon source model which provides us a comparable between three results.

The result of freeze-out geometries shown in figure 6.2 supports the idea of nucleon-antinucleon annihilation suppression from pion enhancement at high ener-
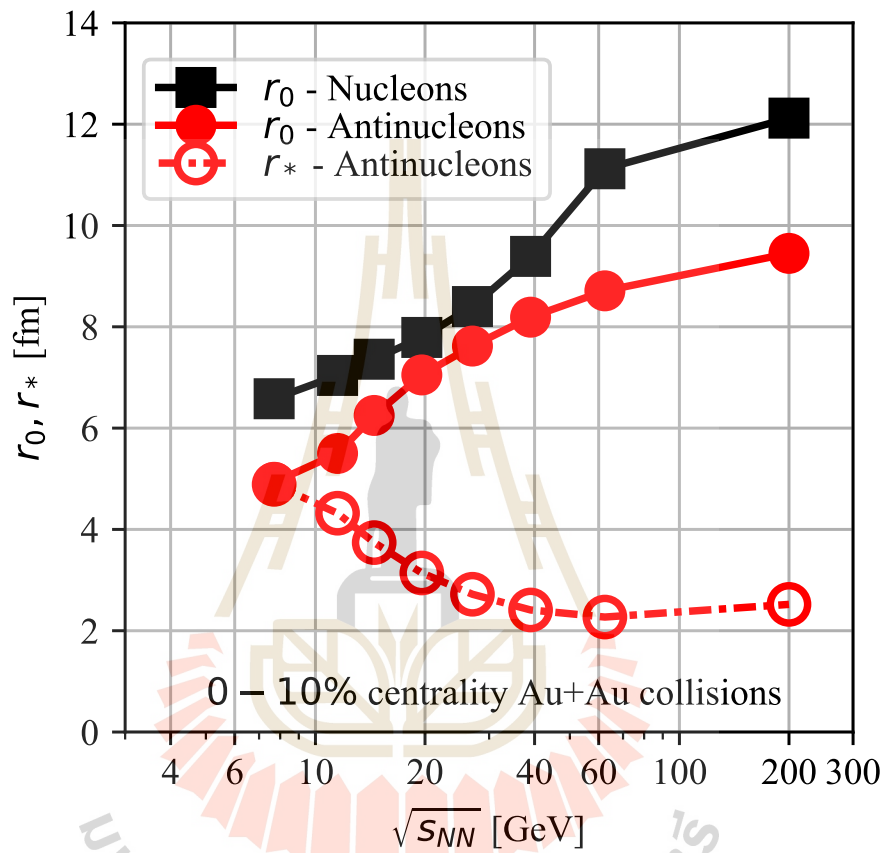
Figure 6.2 The (anti)nucleon source geometry at central $(0-10\%)$ centrality Au+Au collisions (UrQMD) as a function of center-of-mass energy from $\sqrt{s_{NN}} = 7.7 - 200$ GeV. The black square symbols represent the nucleon source. The red cycle symbols represent the antinucleon source. The fireball radius r_0 and suppression radius r_* are indicated by a solid-line and a dashed-line, respectively.
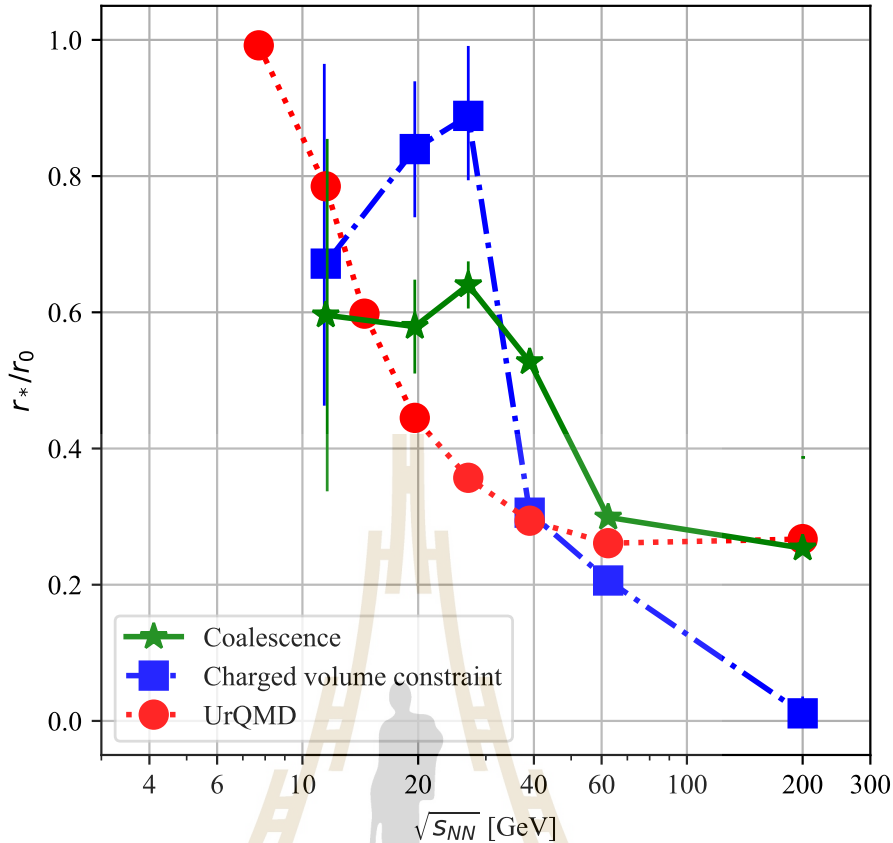
Figure 6.3 The r_*/r_0 ratio of antinucleon source from coalescence model (green star symbol), charged volume constrain (blue square symbol), and UrQMD simulation (red circle symbol).

gies. Furthermore, the fireball volume increases according to the charged volume. However, the fireball radius r_0 from UrQMD is larger than the charged volume and non-suppressed nucleon method by approximately a factor of two, i.e., $7 < r_0 < 12$ fm. Interestingly, the result from UrQMD does not provide any maximum along the curve. Unlike the previous two methods which give us a maximum of suppression radius r_* at 27 GeV. This is the disadvantage of UrQMD since this dynamical model could not simulate the special phenomena of the QGP.

Finally, we present the r_*/r_0 ratio in figure 6.3 for qualitative behavior of (anti)nucleon source from these difference methods. Ideally, we would expect to see a ratio of 1 at the lowest energy since there should be only nucleons in the

fireball. The antinucleons should be completely suppressed. The UrQMD model (red circle symbol) gives us a satisfying result of $r_*/r_0 = 1$ at low energy of 7.7 GeV. Since we need more experimental data for the lower energy range, we cannot predict the low energy behavior from the other two methods. However, the overall trend seems to agree with the curve decreasing towards higher energy. All methods support the idea of pion enhancement which does not only suppress both species, it also relieves the annihilation suppression on antinucleons. At 200 GeV, the r_* of the charged volume method (blue square symbol) drops to zero which contradicts with other methods. The reason is that, we do not assume the limit of $r_*/r_0 = 1$ at low energy. From UrQMD, we could assume that at lower energy, the ratio would be still 1. This means that antinucleons are completely suppressed until 7.7 GeV. Now we can use this energy limit of 7.7 GeV as a representation of low energy to the charged constraint method. We could impose more conditions to the solution such as fixing the $r_*/r_0 \simeq 1$ of antinucleons at 7.7 GeV and re-calculate the proportionality constant. Also, we could fit nucleons from UrQMD with suppression mode $\bar{\mathcal{D}}(r_0, r_*)$. This would give us another condition for the charged volume constrain. Lastly, at 27 GeV, both coalescence model (green stay symbol) and charged volume constraint methods present behavior of maximum suppression. This could be an interesting phenomenon or possibly QGP.

CHAPTER VII

SUMMARY AND CONCLUSION

We studied and compared the (anti)nucleon source geometries as a function of center-of-mass energy. Firstly, we applied the spatial coalescence model together with coalescence parameter B_2 from NA49 and STAR experiments to calculate the (anti)deuteron formation rate $\mathcal{A}$. Then we extract the (anti)nucleon source geometry. We found that at $\sqrt{s_{NN}} = 200$ GeV, the nucleon-antinucleon annihilations are suppressed by pion enhancement. However, the decreasing fireball radius contradicts the predicted charged volume.

We put the constraint to the coalescence model by introducing the proportionality between a cubic-root of number of charged particle and the source RMS-radius, i.e., $0.925 \cdot N_{ch}^{1/3} = \sqrt{\langle r^2(r_0, r_*) \rangle}$. In this method, the nucleon and antinucleon sources are independent of each other and separated. So the interpretation of the fireball radius could be debatable. The satisfying results give an increasing volume along with the energy. Especially at higher energy, the r_0 curve of nucleon and antinucleon align as they share the same fireball radius. However, the (anti)nucleon suppression radii r_* drop to zero at 200 GeV. This means that both species are free from any kind of suppression. But we suspect that the effect of pion enhancement should at least suppress one of two species.

So, we employ the dynamical simulation from UrQMD at $0 - 10\%$ centrality Au+Au collisions from $7.7 - 200$ GeV. The freeze-out (anti)nucleon transverse distribution has been presented. At low energy, the antinucleon source is strongly suppressed at the core of the fireball by the annihilation process while the suppression is very low only around 5% in the case of nucleon source. At 200 GeV, both species are suppressed by $30 - 40\%$. This reflects the effect of pion suppression. How-

ever, for the simplicity, we fit the nucleon and antinucleon distribution with source function of $\mathcal{D}(r_0)$ and $\bar{\mathcal{D}}(r_0, r_*)$ respectively. The result supports the increasing trend of fireball volume along with the energy as predicted by charged volume also the decreasing trend of suppression radius r_* by the pion enhancement. However, with the nature of UrQMD, we can not simulate the special phenomena of a QGP. The smooth curve without the maximum behavior at 27 GeV could be a loss of information which UrQMD could not simulate.

Finally, we show the qualitative comparison between three methods with r_*/r_0 ratio as a function of center-of-mass energy. We found UrQMD gives us an ideal ratio of 1 at 7.7 GeV. This ratio also emphasizes the need for low energy (anti)deuteron coalescence parameter experimental data. We could not obtain the same ratio of 1 for the other two cases. However, this ratio from UrQMD could be put into the charged constraint method as another condition to see how that new extracted sources evolve along with the energy. Lastly, the three curves support the decreasing of antinucleon suppression, this could be understood as a consequence of pion enhancement.
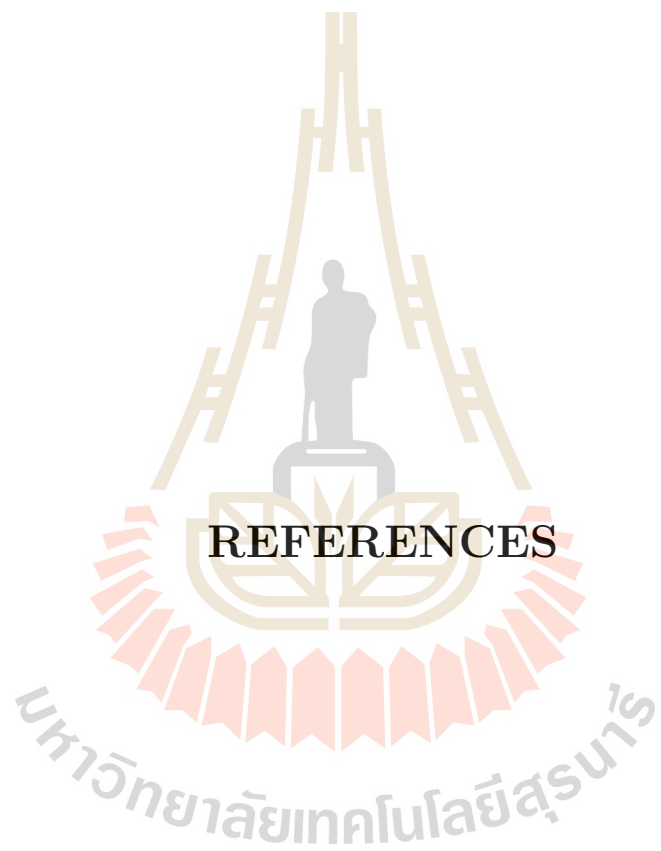
REFERENCES

REFERENCES

Adam, J., Adamczyk, L., Adams, J. R., Adkins, J. K., Agakishiev, G., Aggarwal, M. M., Ahammed, Z., Alekseev, I., Anderson, D. M., Aoyama, R., Aparin, A., Arkhipkin, D., Aschenauer, E. C., Ashraf, M. U., Atetalla, F., et al. (2019). Beam energy dependence of (anti-)deuteron production in Au + Au collisions at the BNL Relativistic Heavy Ion Collider. **Phys. Rev. C** 99(6): 064905.

Adare, A., Afanasiev, S., Aidala, C., Ajitanand, N. N., Akiba, Y., Akimoto, R., Al-Bataineh, H., Alexander, J., Alfred, M., Al-Jamel, A., Al-Ta'ani, H., Angerami, A., Aoki, K., Apadula, N., Aphecetche, L., et al. (2016). Transverse energy production and charged-particle multiplicity at midrapidity in various systems from $\sqrt{s_{NN}} = 7.7$ to 200 GeV. **Phys. Rev. C** 93(2): 024901.

Adler, C., Ahammed, Z., Allgower, C., Anderson, M., Averichev, G. S., Balewski, J., Barannikova, O., Barnby, L. S., Baudot, J., Bekele, S., Belaga, V. V., Bellwied, R., Berger, J., Bichsel, H., Bland, L. C., et al. (2001). Midrapidity Antiproton-to-Proton Ratio from $Au + Au$ Collisions at $\sqrt{s_{\mathrm{NN}}} = 130$GeV. **Phys. Rev. Lett.** 86(21): 4778–4782.

Aichelin, J. and Remler, E. A. (1987). Deuteron and entropy production in relativistic heavy ion collisions. **Phys. Rev. C** 35(4): 1291–1296.

Aid, S., Andreev, V., Andrieu, B., Appuhn, R.-D., Arpagaus, M., Babaev, A., Bähr, J., Bán, J., Ban, Y., Baranov, P., Barrelet, E., Barschke, R., Bartel, W., Barth, M., Bassler, U., et al. (1995). Leptoquarks and compositeness scales from a contact interaction analysis of deep inelastic e±p scattering at HERA. **Phys. Lett. B** 353(4): 578–588.

Alpher, R. A. and Herman, R. (1948). Evolution of the Universe. **Nature** 162(4124): 774–775.

Aoki, M., Beatty, J., Beavis, D., Carroll, J. B., Chiba, J., Crawford, H. J., Debbe, R., Doke, T., Engelage, J., Greiner, L., Hayano, R. S., Hallman, T. J., Heckman, H. H., Kashiwagi, T., Kikuchi, J., et al. (1992). Measurements at 0° of negatively charged particles and antinuclei produced in collisions of 14.6A GeV/c Si on Al, Cu, and Au targets. **Phys. Rev. Lett.** 69(16): 2345–2348.

Armstrong, T. A., Barish, K. N., Batsouli, S., Bennett, S. J., Bertaina, M., Chikanian, A., Coe, S. D., Cormier, T. M., Davies, R., Dover, C. B., Fachini, P., Fadem, B., Finch, L. E., George, N. K., Greene, S. V., et al. (2000). Antideuteron Yield at the AGS and Coalescence Implications. **Phys. Rev. Lett.** 85(13): 2685–2688.

Back, B. B., Baker, M. D., Barton, D. S., Betts, R. R., Bindel, R., Budzanowski, A., Busza, W., Carroll, A., Corbo, J., Decowski, M. P., Garcia, E., George, N., Gulbrandsen, K., Gushue, S., Halliwell, C., et al. (2001). Energy Dependence of Particle Multiplicities in Central Au+Au Collisions. **Phys. Rev. Lett.** 88(2): 022302.

Bass, S., Belkacem, M., Bleicher, M., Brandstetter, M., Bravina, L., Ernst, C., Gerland, L., Hofmann, M., Hofmann, S., Konopka, J., Mao, G., Neise, L., Soff, S., Spieles, C., Weber, H., et al. (1998). Microscopic models for ultrarelativistic heavy ion collisions. **Prog. Part. Nucl. Phys.** 41: 255–369.

Bearden, I., Beavis, D., Besliu, C., Blyakhman, Y., Brzychczyk, J., Budick, B., Bøggild, H., Chasman, C., Christensen, C., Christiansen, P., Cibor, J., Debbe, R., Gaardhøje, J., Grotowski, K., Hagel, K., et al. (2001). Rapidity dependence of antiproton-to-proton ratios in Au+Au collisions at square root of (sNN) = 130 GeV. **Phys. Rev. Lett.** 87(11): 112305.

Beyer, M. (1993). Test of time-reversal symmetry in the proton-deuteron system. **Nucl. Phys. A** 560(4): 895–908.

Bjorken, J. D. (1983). Highly relativistic nucleus-nucleus collisions: The central rapidity region. **Phys. Rev. D** 27(1): 140–151.

Bleicher, M., Zabrodin, E., Spieles, C., Bass, S. A., Ernst, C., Soff, S., Bravina, L., Belkacem, M., Weber, H., Stöcker, H., and Greiner, W. (1999). Relativistic hadron-hadron collisions in the ultra-relativistic quantum molecular dynamics model. **J. Phys. G: Nucl. Part. Phys.** 25(9): 1859–1896.

Bleicher, M., Hillmann, P., Reichert, T., Steinheimer, J., Sombun, S., Herold, C., Limphirat, A., and Yan, Y. (2020). Transport model calculations of deuteron production in relativistic hadron and heavy-ion collisions. **Astronomische Nachrichten** 340(9-10): 977–982.

Braun-Munzinger, P., Magestro, D., Redlich, K., and Stachel, J. (2001). Hadron production in Au–Au collisions at RHIC. **Phys. Lett. B** 518(1-2): 41–46.

Braun-Munzinger, P. and Dönigus, B. (2019). Loosely-bound objects produced in nuclear collisions at the LHC. **Nucl. Phys. A** 987: 144–201.

Braun-Munzinger, P., Redlich, K., and Stachel, J. (2004). Particle production in heavy ion collisions. **Quark–Gluon Plasma 3**. World Scientific, 491–599.

Busza, W., Rajagopal, K., and Schee, W. van der (2018). Heavy Ion Collisions: The Big Picture and the Big Questions. **Annu. Rev. Nucl. Part. Sci.** 68(1): 339–376.

Butler, S. T. and Pearson, C. A. (1961). Deuterons from High-Energy Proton Bombardment of Matter. **Phys. Rev. Lett.** 7(2): 69–71.

Cabibbo, N. and Parisi, G. (1975). Exponential hadronic spectrum and quark liberation. **Phys. Lett. B** 59(1): 67–69.

Chen, J., Keane, D., Ma, Y.-G., Tang, A., and Xu, Z. (2018). Antinuclei in heavy-ion collisions. **Phys. Rept.** 760: 1–39.

Chen, L.-W., Ko, C., and Li, B.-A. (2003). Light cluster production in intermediate energy heavy-ion collisions induced by neutron-rich nuclei. **Nucl. Phys. A** 729(2): 809–834.

DeGrand, T. A. (1984). Are antibaryons a signal for a phase transition in ultrarelativistic nucleus-nucleus collisions? **Phys. Rev. D** 30(9): 2001–2004.

Dover, C. B., Heinz, U., Schnedermann, E., and Zimányi, J. (1991). Covariant coalescence model for relativistically expanding systems. **Phys. Rev. C** 44(4): 1636–1654.

Fehling, D. (2008). The standard model of particle physics: A lunchbox's guide. **The Johns Hopkins University, Retrieved on**: 12–03.

Fritzsch, H. and Gell-Mann, M. (1972). Current algebra: Quarks and what else? **eConf** C720906V2. Ed. by J. D. Jackson and A. Roberts: 135–165. arXiv: `hep-ph/0208010`.

Gosset, J., Gutbrod, H. H., Meyer, W. G., Poskanzer, A. M., Sandoval, A., Stock, R., and Westfall, G. D. (1977). Central collisions of relativistic heavy ions. **Phys. Rev. C** 16(2): 629–657.

Hagedorn, R. (1960). Deuteron Production in High-Energy Collisions. **Phys. Rev. Lett.** 5(6): 276–277.

Herold, C., Kittiratpattana, A., Kobdaj, C., Limphirat, A., Yan, Y., Nahrgang, M., Steinheimer, J., and Bleicher, M. (2019). Entropy production and reheating at the chiral phase transition. **Phys, Lett. B** 790: 557–562.

Hodgson, P. E. (1971). Nuclear reactions and nuclear structure. 426.

Hou, S. Q., He, J. J., Parikh, A., Kahl, D., Bertulani, C. A., Kajino, T., Mathews, G. J., and Zhao, G. (2017). Non-extensive Statistics Solution to the Cosmological Lithium Problem. **ApJ** 834(2): 165.

Jennings, B. K., Gupta, S. D., and Mobed, N. (1982). Aspects of deuteron production in relativistic heavy ion collisions. **Phys. Rev. C** 25(1): 278–285.

Kabana, S., Ambrosini, G., Arsenescu, R., Baglin, C., Beringer, J., Borer, K., Bussière, A., Dittus, F., Elsener, K., Gerber, B., Gorodetzky, P., Guillaud, J., Hess, P., Kabana, S., Klingenberg, R., et al. (1998). New results from NA52 on particle

production in Pb+Pb collisions at 158 GeV per nucleon. **Nucl. Phys. A** 638(1): 411c–414c.

Kapusta, J. I. (1980). Mechanisms for deuteron production in relativistic nuclear collisions. **Phys. Rev. C** 21(4): 1301–1310.

Korsmeier, M., Donato, F., and Fornengo, N. (2018). Prospects to verify a possible dark matter hint in cosmic antiprotons with antideuterons and antihelium. **Phys. Rev. D** 97(10): 103011.

Leupold, S. and Heinz, U. (1994). Coalescence model for deuterons and antideuterons in relativistic heavy-ion collisions. **Phys. Rev. C** 50(2): 1110–1128.

Malaney, R. A. and Mathews, G. J. (1993). Probing the early universe: a review of primordial nucleosynthesis beyond the standard big bang. **Phys. Rept.** 229(4): 145–219.

Martinez, G. (2013). **Advances in Quark Gluon Plasma**. arXiv: `1304.1452 [nucl-ex]`.

McInnes, B. (2016). A rotation/magnetism analogy for the quark–gluon plasma. **Nucl. Phys. B** 911: 173–190.

McLerran, L. and Pisarski, R. D. (2007). Phases of dense quarks at large Nc. **Nucl. Phys. A** 796(1-4): 83–100.

Mekjian, A. Z. (1978). Explosive nucleosynthesis, equilibrium thermodynamics, and relativistic heavy-ion collisions. **Phys. Rev. C** 17(3): 1051–1070.

Mekjian, A. (1977). Thermodynamic Model for Composite-Particle Emission in Relativistic Heavy-Ion Collisions. **Phys. Rev. Lett.** 38(12): 640–643.

Monnai, A. (2014). **Relativistic dissipative hydrodynamic description of the quark-gluon plasma**. Springer Science & Business Media.

Monreal, B., Bass, S., Bleicher, M., Esumi, S., Greiner, W., Li, Q., Liu, H., Llope, W., Mattiello, R., Panitkin, S., Sakrejda, I., Snellings, R., Sorge, H., Spieles, C.,

Stoecker, H., et al. (1999). Deuterons and space-momentum correlations in high energy nuclear collisions. **Phys. Rev. C** 60(3): 031901.

Mrówczyński, S. (1993). Anti-nucleon sources in heavy ion collisions. **Phys. Lett. B** 308: 216–219.

Mrówczyński, S. (1990). Antideuteron production and the size of the interaction zone. **Phys. Lett. B** 248(3-4): 459–463.

Mrówczyński, S. (2017). Production of Light Nuclei in the Thermal and Coalescence Models. **Acta Phys. Polon. B** 48(4): 707.

Nagle, J., Kumar, B., Kusnezov, D., Sorge, H., and Mattiello, R. (1996). Coalescence of deuterons in relativistic heavy ion collisions. **Phys. Rev. C** 53(1): 367.

Oh, Y. and Ko, C. M. (2007). Elliptic flow of deuterons in relativistic heavy-ion collisions. **Phys. Rev. C** 76(5): 054910.

Oliinychenko, D. (2021). Overview of light nuclei production in relativistic heavy-ion collisions. **Nucl. Phys. A** 1005: 121754.

Rufa, M., Schaffner, J., Maruhn, J., Stöcker, H., Greiner, W., and Reinhard, P.-G. (1990). Multi-lambda hypernuclei and the equation of state of hypermatter. **Phys. Rev. C** 42(6): 2469.

Sarkar, S., Satz, H., and Sinha, B. (2009). **The physics of the quark-gluon plasma: introductory lectures**. Vol. 785. Springer.

Sato, H. and Yazaki, K. (1981). On the coalescence model for high energy nuclear reactions. **Phys. Lett. B** 98(3): 153–157.

Schaffner-Bielich, J. and Gal, A. (2000). Properties of strange hadronic matter in bulk and in finite systems. **Phys. Rev. C** 62(3): 034311.

Shi, S., Adam, J., Adamczyk, L., Adams, J. R., Adkins, J. K., Agakishiev, G., Aggarwal, M. M., Ahammed, Z., Alekseev, I., Anderson, D. M., Aoyama, R., Aparin, A., Arkhipkin, D., Aschenauer, E. C., Ashraf, M. U., et al. (2009). Event anisotropy ν_2 at STAR. **Nucl. Phys. A** 830(1-4): 187c–190c.

Soff, S. (2002). HBT interferometry and the parton-hadron phase transition. **arXiv preprint hep-ph/0202240**.

Sombun, S., Tomuang, K., Limphirat, A., Hillmann, P., Herold, C., Steinheimer, J., Yan, Y., and Bleicher, M. (2019). Deuteron production from phase-space coalescence in the UrQMD approach. **Phys. Rev. C** 99(1): 014901.

Specht, H. (2002). Experimental conference summary. **Nucl. Phys. A** 698(1-4): 341–359.

Steinheimer, J., Gudima, K., Botvina, A., Mishustin, I., Bleicher, M., and Stöcker, H. (2012). Hypernuclei, dibaryon and antinuclei production in high energy heavy ion collisions: thermal production vs. coalescence. **Phys. Lett. B** 714(1): 85–91.

Stephanov, M., Rajagopal, K., and Shuryak, E. (1998). Signatures of the tricritical point in QCD. **Phys. Rev. Lett.** 81(22): 4816.

Sun, K.-J., Chen, L.-W., Ko, C. M., Pu, J., and Xu, Z. (2018). Light nuclei production as a probe of the QCD phase diagram. **Phys. Lett. B** 781: 499–504.

Sun, K.-J. and Ko, C. M. (2020). Light nuclei production in relativistic heavy ion collisions from the AMPT model. **arXiv preprint arXiv:2005.00182**.

Van Buren, G., Armstrong, T., Barish, K. N., Batsouli, S., Bennett, S. J., Bertaina, M., Chikanian, A., Coe, S. D., Cormier, T. M., Davies, R., Dover, C. B., Fachini, P., Fadem, B., Finch, L. E., George, N. K., et al. (1999). Antideuteron yield and coalescence implications at the AGS. **Nucl. Phys. A** 661(1-4): 391–394.

Wiringa, R. B., Schiavilla, R., Pieper, S. C., and Carlson, J. (2014). Nucleon and nucleon-pair momentum distributions in A12 nuclei. **Phys. Rev. C** 89(2): 024305.

Xu, N. (2018). Exploration of the QCD Phase Diagram at Finite Baryon Density Region: Recent. **XXII DAE High Energy Physics Symposium: Proceedings**. Vol. 203. Springer.

Xu, Z.-b., Adam, J., Adamczyk, L., Adams, J. R., Adkins, J. K., Agakishiev, G., Aggarwal, M. M., Ahammed, Z., Alekseev, I., Anderson, D. M., Aoyama, R., Aparin,

A., Arkhipkin, D., Aschenauer, E. C., Ashraf, M. U., et al. (2001). Resonance studies at STAR. **Nucl. Phys. A** 698: 607–610.

Zhu, L., Ko, C. M., and Yin, X. (2015). Light (anti-) nuclei production and flow in relativistic heavy-ion collisions. **Phys. Rev. C** 92(6): 064911.
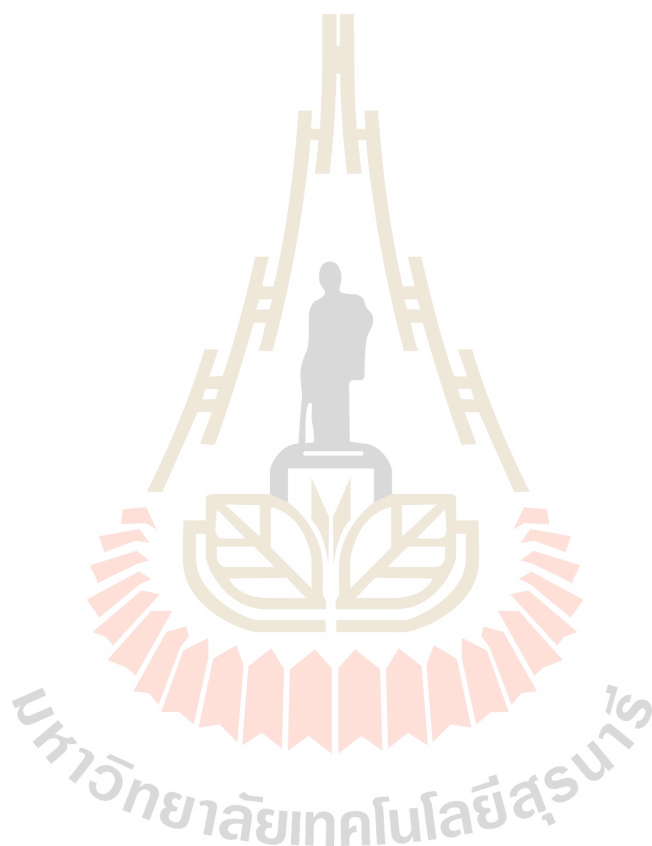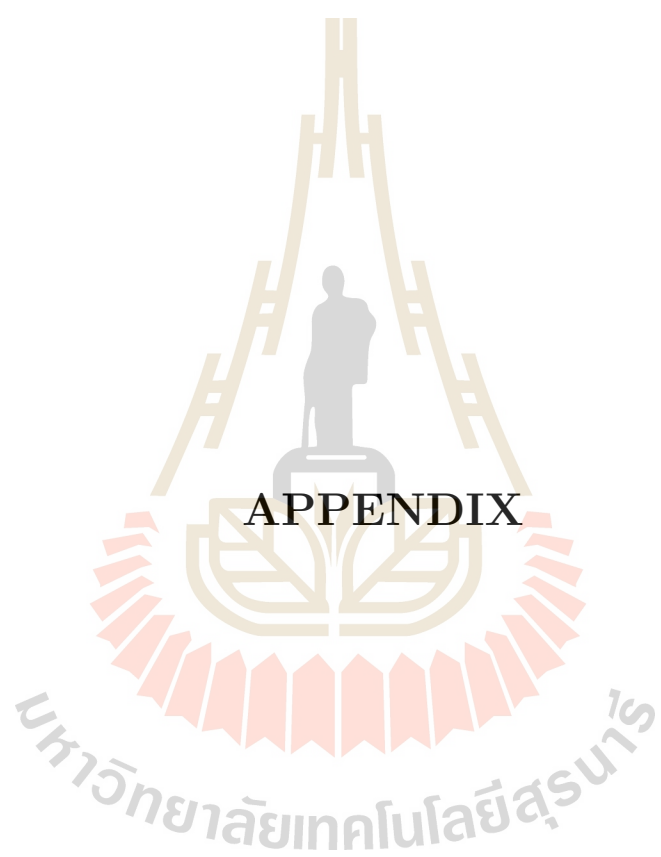
APPENDIX

APPENDIX

UNIT AND NOTATIONS

We work in units where $c = h = k_B = 1$. With the relations

$$x = ct, \tag{1}$$

$$hk = p, \tag{2}$$

$$E = k_B T, \tag{3}$$

In particle physics, the space x and time t and momentum p as well as energy E and temperature T are all in the same dimensions i.e. fm (femtometer or fermi) and MeV (mega electron volt) respectively. These two are also equivalent and can be transformed into each other via

$$1 = hc = 197.3 \ \text{MeVfm} \tag{4}$$

The relations to usual SI-units are 1 fm $= 10^{-15}$ m and 1 MeV $= 1.602 \cdot 10^{-13}$ J. The constants are the speed of light $c = 2.99792458 \cdot 10^8$ m/s, the Planck constant $h = 1.055 \cdot 10^{-34}$ Js and the Boltzmann constant $k_B = 1.381 \cdot 10^{-23}$ J/K.

CIRRICULUM VITAE

Name: Apiwit Kittiratpattana

Date Birth: 24 February 1996

Place of Birth: Nakhon Ratchasima, Thailand

E-mail: apiwitkitti@g.sut.ac.th

Education: (Jun 2557 – May 2561) – Physics, Bachelor of Science, Suranaree University of Technology (SUT), Nakhon Ratchasima, Thailand

(Jun 2561 - Present) – Physics, Master of Science, Suranaree University of Technology, Nakhon Ratchasima, Thailand

Publications: (2020) – "Deuteron and Antideuteron Coalescence in Heavy-Ion Collisions: Energy Dependence of the Formation Geometry." Kittiratpattana, A., Wondrak, M. F., Hamzic, M., Bleicher, M., Herold, C., & Limphirat, A. **The European Physical Journal A**, 56(10), 1-6

(2019) – "Entropy Production and Reheating at the Chiral Phase Transition." Herold, C., Kittiratpattana, A., Kobdaj, C., Limphirat, A., Yan, Y., Nahrgang, M., … & Bleicher, M. **Physics Letters B,** 790, 557-562.

Grants and Fellowships: (2557 - Present) – Development and Promotion of Science and Technology Talents Project (DPST)